

# The Temperature Distribution of Dense Molecular Gas in the Center of NGC 253

Jürgen Ott<sup>1</sup>

*CSIRO Australia Telescope National Facility, Cnr Vimiera & Pembroke Roads, Marsfield NSW 2122, Australia*

[Juergen.Ott@csiro.au](mailto:Juergen.Ott@csiro.au)

Axel Weiß

*Instituto de Radio Astronomía Milimétrica, Avenida Divina Pastora 7, 18012 Granada, Spain*

[aweiss@iram.es](mailto:aweiss@iram.es)

Christian Henkel

*Max-Planck-Institut für Radioastronomie, Auf dem Hügel 69, 53121 Bonn, Germany*

[chenkel@mpifr-bonn.mpg.de](mailto:chenkel@mpifr-bonn.mpg.de)

and

Fabian Walter

*Max-Planck-Institut für Astronomie, Königstuhl 17, 69117 Heidelberg, Germany*

[walter@mpia.de](mailto:walter@mpia.de)

## ABSTRACT

We present interferometric maps of ammonia ( $\text{NH}_3$ ) of the nearby starburst galaxy NGC 253. The observations have been taken with the Australia Telescope Compact Array and include the para- $\text{NH}_3$  (1,1), (2,2), and the ortho- $\text{NH}_3$  (3,3) and (6,6) inversion lines. Six major complexes of dense ammonia are identified, three of them on either side of the starburst center, out to projected galactocentric radii of  $\sim 250$  pc. Rotational temperatures are derived toward selected individual positions as well as for the entire south-eastern and north-western molecular complexes. The application of radiative transfer large velocity gradient models reveals that the bulk of the ammonia molecules is embedded in a one-temperature

gas phase. Kinetic temperatures of this gas are  $\sim$ 200 and 140 K toward the south-west and north-east, respectively. The temperatures under which ammonia was formed in the past are with  $\gtrsim$ 30 K also warmer toward the south-west than toward the north-east ( $\sim$  15 – 20 K). This is indicated by the ortho-to-para ammonia ratio which is  $\sim$  1 and 1.5 – 2.5 toward the south-west and north-east, respectively. Ammonia column densities in the brightest complexes are in the range of  $6 – 11 \times 10^{14} \text{ cm}^{-2}$ , which adds up to a total ammonia mass of  $\sim 20 M_{\odot}$ , about evenly distributed toward both sides of the nucleus. Ammonia abundances relative to H<sub>2</sub> are  $\sim 3 \times 10^{-8}$ . In the south-western complex, the ammonia abundances increase from the starburst center to larger galactocentric radii. Toward the center of NGC 253, NH<sub>3</sub>(1,1), (2,2), and (6,6) is detected in absorption against an unresolved continuum source. At the same location, however, ammonia (3,3) is found in emission which indicates maser activity. This would be the first detected extragalactic NH<sub>3</sub> maser. Evidence for an expanding shell in the south-western complex is provided. The shell, with a dynamical age of  $\sim 1.3 \text{ Myr}$ , is centered on an X-ray point source which must be located within the dense gas of NGC 253. The shell and X-ray properties can be reproduced by the energy input of a highly obscured young stellar cluster with a mass of  $\sim 10^5 M_{\odot}$  which also heats the dense gas. A current star formation rate of  $\sim 2.8 M_{\odot} \text{ yr}^{-1}$  is derived for the nuclear starburst in NGC 253 based on its 1.2 cm continuum emission.

*Subject headings:* galaxies: individual (NGC 253) — galaxies: starburst — galaxies: ISM — galaxies: nuclei — ISM: molecules — radio lines: galaxies

NGC 253

## 1. Introduction

Starburst galaxies are a main contributor to the star formation (SF) in the universe ( $\sim 20\%$  at  $z < 0.2$ ; Brinchmann et al. 2004). The fuel for star formation is dense molecular gas. Recently Gao & Solomon (2004) showed that in actively star forming galaxies the molecular gas with volume densities  $> 10^4 \text{ cm}^{-3}$  (traced by HCN) correlates very well with the SF rate (SFR) determined by the far-infrared (FIR) emission. Less dense molecular gas,

---

<sup>1</sup>Bolton Fellow

such as that traced by CO, is a weaker measure of the current SFR. The physical state of the molecular gas is mainly described by its temperature and density. It is thus important to constrain the range of those two fundamental parameters to understand how molecular gas feeds regions of massive SF in nuclear environments.

Tracers for high density molecular gas are transitions of molecules with large electric dipole moments (relative to CO), such as HCN,  $\text{HCO}^+$ , CS, or ammonia ( $\text{NH}_3$ ). Those molecules are excited at densities  $\gtrsim 10^4 \text{ cm}^{-3}$ , which we refer to as *dense* gas. The specific tetrahedral structure of ammonia that permits the tunneling of the nitrogen atom through the plane defined by the three hydrogen atoms causes inversion doublets. Since the energy difference between the two states of a given inversion doublet does only weakly depend on the rotational quantum numbers  $J$  and  $K$ , a vast range of molecular excitation can be covered with just one set of radio receivers.

For the metastable ( $J=K$ ) inversion lines, at the bottom of each  $K$ -ladder, radiative decay is extremely slow and the rotation temperature  $T_{\text{rot}}$  (the temperature defined by the populations of the different rotational levels) is to first order similar to the kinetic temperature ( $T_{\text{kin}}$ ) of the dense molecular gas (e.g., Ho & Townes 1983; Walmsley & Ungerechts 1983; Stutzki & Winnewisser 1985; Martin & Ho 1986; Ungerechts, Winnewisser, & Walmsley 1986; Danby et al. 1988; Flower, Pineau des Forets, & Walmsley 1995; Hüttemeister et al. 1995). Deviations between  $T_{\text{rot}}$  and  $T_{\text{kin}}$  at higher temperatures are well described by radiative transfer large velocity gradient (LVG) models. Ammonia is the brightest molecular species with those properties which makes it an important and easy-to-use thermometer. According to the orientation of the hydrogen spins, two different variants of ammonia can be distinguished: ortho- $\text{NH}_3$  (all three hydrogen spins are parallel) and para- $\text{NH}_3$  (one spin is anti-parallel). This restricts the rotational ( $J, K$ ) states to  $K = 3n$  ( $n$  is an integer,  $J$  the quantum number of the total angular momentum,  $K$  its projection onto the symmetry axis of the molecule) for ortho and  $K \neq 3n$  for para-ammonia (e.g., Townes & Schawlow 1955; Ho & Townes 1983). Since the lowest state of ammonia belongs to ortho-ammonia, an ortho-to-para-ammonia ratio exceeding unity is expected if the formation and equilibration of  $\text{NH}_3$  is performed in an environment with a low energy content (e.g., Takano, Nakai, & Kawaguchi 2002).

Up to now, rotational ammonia temperatures in extragalactic objects were only derived from single dish observations (e.g., Martin & Ho 1986; Henkel et al. 2000; Takano et al. 2000; Weiß et al. 2001a; Takano, Nakai, & Kawaguchi 2002; Mauersberger et al. 2003) which restricted the temperature measurements to global averages over a few hundred pc. The only interferometric (VLA) extragalactic ammonia maps were presented by Ho et al. (1990) for IC 342. The signal-to-noise ratio of these maps, however, was not good enough for

temperature determinations. In this paper we present interferometric maps of ammonia toward the core of the galaxy NGC 253 observed with the Australia Telescope Compact Array (ATCA). The observations have a linear resolution of  $\sim 5''$  (corresponding to 65 pc) along the major axis and are therefore a clear improvement over single dish observations presented by Takano, Nakai, & Kawaguchi (2002) (hereafter T02) and Mauersberger et al. (2003) (M03). NGC 253 is one of the most nearby starburst galaxies (distance adopted here: 2.6 Mpc, Puche & Carignan 1988; but see Karachentsev et al. 2003: 3.9 Mpc). The current SFR of  $\sim 3 M_{\odot} \text{ yr}^{-1}$  (Radovich, Kahanpää, & Lemke 2001) is mainly concentrated in the inner  $\sim 200$  pc. The starburst, likely fed by gas streaming toward the center along a prominent bar, is visible at virtually all wavelengths (e.g., Ulvestad & Antonucci 1997; Engelbracht et al. 1998; Forbes et al. 2000; Strickland et al. 2002; Jarrett et al. 2003). Furthermore, feedback from massive stars in the form of strong stellar winds and supernova explosions heats the surrounding gas and a galactic wind is observable in NGC 253 up to 8 kpc above the disk (Strickland et al. 2002). Molecular lines have been abundantly found toward the nucleus of NGC 253 (e.g., Turner 1985; Jackson et al. 1995; Houghton et al. 1997; García-Burillo et al. 2000; Bradford et al. 2003; Mauersberger et al. 2003; Martín et al. 2003; Paglione et al. 2004; Henkel et al. 2004; Bayet et al. 2004) and, in fact, almost every molecule which was detected in an extragalactic object has also been detected in NGC 253.

In Sect. 2 we describe the observational parameters of our ATCA ammonia data as well as the data reduction techniques. This is followed by the presentation of the data in Sect. 3. We discuss the ammonia and continuum observations in Sect. 4 and summarize the paper in Sect. 5.

## 2. Observations and Data Analysis

Observations of the para- $\text{NH}_3$  (1,1) and (2,2) inversion lines were simultaneously performed with the ATCA on 2003 September 05. On 2004 April 26, the ATCA was used to simultaneously observe ortho- $\text{NH}_3$  (3,3) and (6,6). During both observations, the ATCA was in the compact EW 367 array configuration. The bandwidths were chosen to be 64 MHz for each line, centered on the redshifted frequencies of 23.6755, 23.7035, 23.851, and 25.036 GHz, respectively (primary half-power beam widths:  $\sim 2.2'$ ). Each of the frequency bands were split into 64 channels resulting in a channel width of 1 MHz or  $\sim 12.65 \text{ km s}^{-1}$  ( $\sim 11.96 \text{ km s}^{-1}$  in the case of the  $\text{NH}_3$  (6,6) line). For the calibration of the  $\text{NH}_3$  (1,1) and (2,2) observations we used Uranus as a flux calibrator, PKS 1921-293 as a bandpass calibrator (integration time  $\sim 10$  min), and PKS 0023-263 as a phase calibrator (4 min after each 20 min observing interval on NGC 253). The calibrators for the  $\text{NH}_3$  (3,3) and (6,6) observations were the same

except that PKS 1934-638 was used to determine the flux scales. Calibration uncertainties are estimated to be  $\sim 10\%$ . Due to the lower signal-to-noise ratio of the  $\text{NH}_3(6,6)$  line, we estimate the error for this line to  $\sim 20\%$ . Relative uncertainties between the different line fluxes do not depend on absolute calibration errors and are  $\sim 5\%$ . The total  $\text{NH}_3(1,1)$  and  $(2,2)$  integration time on NGC 253 was  $\sim 8.5$  h spread over a 12 h interval yielding a good uv-coverage of the east-west interferometer. The  $\text{NH}_3(3,3)$  and  $(6,6)$  integration time was  $\sim 6$  hours spread over  $\sim 7$  hours. This resulted in a reduced uv-coverage. Both, the XX and the YY polarizations were observed at all frequencies.

The data were reduced with the MIRIAD (Sault, Teuben, & Wright 1995) and visualized with the KARMA (Gooch 1996) software packages. After flagging very few corrupted visibilities and discarding edge channels, calibration was applied to the data. Subsequently, the data were Fourier transformed to image data cubes with a gridding of  $1''$  pixel size. Along with the transform, we used natural weighting which results in a synthesized beam of  $18''.8 \times 5''.2$  in size (position angle:  $-0.7^\circ$ ) for the full uv-coverage  $\text{NH}_3(1,1)/(2,2)$  data. Continuum maps were produced by averaging line-free channels. Due to sidelobes of the strong emission, the rms noise of the naturally weighted continuum maps is with  $\sim 1 \text{ mJy beam}^{-1}$  at 23.6755 and 23.7035 GHz and  $\sim 1.5 \text{ mJy beam}^{-1}$  at 23.851 and 25.036 GHz about twice that of the continuum-subtracted channel maps (see below). The continuum maps were subtracted from all channel maps to obtain continuum-free line cubes. Since the uv-coverages of the  $\text{NH}_3(1,1)/(2,2)$  and  $\text{NH}_3(3,3)/(6,6)$  cubes differ we also produced  $(1,1)$  and  $(2,2)$  data cubes restricted to the hour angles set by the  $\text{NH}_3(3,3)/(6,6)$  observations. This resulted in a synthesized beam of  $30''.41 \times 5''.09$  and a position angle of  $-12^\circ$ , which is almost orthogonal to the distribution of the dense gas as seen, e.g., in Peng et al. (1996). The data was Hanning smoothed (which resulted in a velocity resolution about twice the channel width) and CLEANed down to a  $1 \text{ mJy}$  level (about  $2\sigma$  rms noise).

For a proper comparison of the line properties, the  $\text{NH}_3(6,6)$  and the LST restricted  $(1,1)/(2,2)$  cubes were finally smoothed to the spatial resolution of the  $\text{NH}_3(3,3)$  data. The channel maps of all data cubes exhibit an rms noise of  $\sim 0.6 \text{ mJy beam}^{-1}$ . We also produced a super-resolved cube of  $\text{NH}_3(3,3)$  by convolving the CLEAN components with a circular beam of  $5'' \times 5''$ . The super-resolved cube is not used for any quantitative analysis but provides a better morphological separation of individual clumps of dense molecular gas. Moment maps were computed by selecting only emission components with a signal at least 2.5 times above the rms per channel map. In addition, the signal must be visible in at least three consecutive channels to be incorporated. All other data was flagged before producing the integrated intensity, the intensity weighted velocity, and the velocity dispersion maps (i.e., Moments 0, 1, and 2).

### 3. Results

#### 3.1. Continuum Emission

Spatially unresolved continuum emission was detected in all bands toward the central starburst of NGC 253 at  $\alpha_{(J2000)} = 00^h 47^m 33\rlap{.}^s 2$ ,  $\delta_{(J2000)} = -25^\circ 17' 17''$ . The flux density of the continuum source is derived to 520 mJy with an absolute uncertainty of  $\sim 10\%$ . The flux is in good agreement with the 31.4 GHz flux of  $(590 \pm 80)$  mJy reported by Geldzahler & Witzel (1981). The relative uncertainty of the continuum fluxes in the four different bands (assuming a flat spectrum within the narrow frequency range) is only  $\sim 5\%$ .

#### 3.2. Global Morphology and Velocity Field of the Ammonia Inversion Lines

The resulting ammonia data cubes are shown as channel maps in Figs. 1 and 2. Note that for these figures the full uv-coverage data of the  $\text{NH}_3$  (1,1) and (2,2) data are used. All ammonia lines are detected and two major complexes, separated spatially and in velocity space can be defined: one toward the north-east (NE) and a second one toward the south-west (SW) of the starburst center. At the starburst center itself, a faint absorption component in  $\text{NH}_3$  (1,1), (2,2), and (6,6) and some broad (3,3) emission are detected against the 1.2 cm radio continuum (Sect. 3.1). The NE component covers a velocity of  $\sim 100 - 240 \text{ km s}^{-1}$  in the LSR system (systemic LSR velocity of NGC 253:  $234 \pm 2 \text{ km s}^{-1}$ ; Whiting 1999) whereas the SW part covers  $\sim 240 - 380 \text{ km s}^{-1}$ . The total  $\text{NH}_3$  spectra, encompassing both the SW and the NE components, are shown in Fig. 3 and their properties are listed in Table 1. A comparison with the single dish observations of M03 and T02 shows that all flux has been recovered by the ATCA observations. In Fig. 3 we overlay a CO spectrum for comparison. The CO data was observed with the Owens Valley Radio Interferometer (courtesy of M. Dahlem and F. Walter) and was smoothed to the ATCA beam of our observations. The  $\text{NH}_3$  spectra of NGC 253 are very similar to those of CO with the high velocity SW component to be about twice as bright as the lower velocity NE component. However, the spectra deviate near the systemic velocity, i.e., close to the starburst center where ammonia appears to be less abundant than at larger galactocentric radii (see Sect. 4.4.4). In addition, the  $\text{NH}_3$  (3,3) line exhibits two components with similar flux levels. This behavior is also visible in the integrated intensity maps shown in Fig. 4. In addition to the spectral similarities, the morphologies of the  $\text{NH}_3$  (1,1), (2,2), and (6,6) inversion lines are very similar, too. The most central NE  $\text{NH}_3$  (3,3) peak, however, is shifted slightly closer to the starburst center as compared to the peaks seen in all other inversion lines. The separation of the (3,3) emission from the other inversion lines in that region is about the extent of the minor axis beam

( $\sim 5''$ ) and is therefore significant (Fig. 4[b]). Such spectral and morphological differences of the  $\text{NH}_3$  (3,3) line are somewhat surprising, as both the (3,3) and (6,6) lines are emitted by ortho- $\text{NH}_3$  (see Sect. 4.2).

Toward the SW region of NGC 253 the intensity weighted, first moment velocity field is rather regular and increases with rising galactocentric distance from  $v_{\text{LSR}} \sim 240$  to  $380 \text{ km s}^{-1}$ . The situation is somewhat different in the NE; the  $\text{NH}_3$  velocities decline from  $v \sim 200$  to  $150 \text{ km s}^{-1}$  at a distance of about  $8''$  from the central starburst region and then rise again to values of  $\sim 200 \text{ km s}^{-1}$ . This trend is already visible in the intensity weighted velocity maps in Fig. 4 but becomes more prominent in the position-velocity (pV) diagram shown in Fig. 5. Linewidths are  $\sim 40 - 90 \text{ km s}^{-1}$ , irrespective of galactocentric radius (see Fig. 4 and Table 2).

## 4. Discussion

### 4.1. The Star Formation Rate in the Nucleus of NGC 253

Ulvestad & Antonucci (1997) showed that most of the radio continuum in the center of NGC 253 is emitted by H II regions and supernova remnants and that no clear evidence for an AGN exists. Therefore, the measured 1.2 cm radio continuum emission can be used to estimate SFRs. To do so, we use the equations given in Haarsma et al. (2000) (see also Condon 1992) and, using the 1.2 cm continuum flux of  $(520 \pm 52) \text{ mJy}$ , we derive the nuclear SFR of NGC 253 to  $(2.8 \pm 0.3) \text{ M}_\odot \text{ yr}^{-1}$ . This is in excellent agreement with far-infrared data ( $\text{SFR}_{\text{FIR}} = 2.6 - 3.3 \text{ M}_\odot \text{ yr}^{-1}$ ; Radovich, Kahanpää, & Lemke 2001).

### 4.2. Properties of Individual Dense Gas Clumps

In the super-resolved data cubes (Fig. 5[a]) six clumps can be identified: clumps A, B, and C are located toward the SW and clumps D, E, and F toward the NE. Only clumps C and D, however, are symmetrical in position and velocity to the starburst center. No symmetry is observed between complexes E/F and A/B. This indicates that an inner ring rotating like a solid body may exist but no such structure can explain the velocity field at larger radii of  $\sim 200 \text{ pc}$ . The SiO and  $\text{H}^{13}\text{CO}^+$  distributions are similar to that of  $\text{NH}_3$  and García-Burillo et al. (2000) interpret the two inner clumps being at the inner Lindblad resonance whereas the outer clumps are the vertices of the trailing spiral arms across the outer Lindblad resonance. This interpretation can potentially explain the kinematic asymmetry of the outer parts of the dense gas. The morphology and kinematics of the  $\text{NH}_3$  complexes are also in

general agreement with CS data (a different tracer for dense gas) presented in Peng et al. (1996). Clumps with CS emission which may be attributed to the ammonia complexes E and F, however, are shifted  $\sim 5''$  toward the center with respect to  $\text{NH}_3$ . Peng et al. (1996) show that some CS emission in the SW, the receding part of NGC 253, is below the systemic velocity. Toward the approaching NE region some gas is found with velocities above the systemic velocity. They explain those features as signatures ( $x_1$  and  $x_2$  orbits) of dense gas moving in a bar potential (see also Sorai et al. 2000; Das, Anantharamaiah, & Yun 2001). Our  $\text{NH}_3$  data do not show those specific signatures, which, however, may be due to the weakness of the emission toward those regions.

Measured from the starburst center, the ammonia emission extends  $\sim 200$  pc toward the NE and  $\sim 250$  pc toward the SW. We define eight positions for a more detailed analysis: Positions P1 to P3 correspond to the centers of clumps A, B, and C and P4 is located on the 1.2 cm continuum emission. In order to account for the small displacement of the  $\text{NH}_3$  (3,3) emission with respect to the other inversion lines in the innermost NE complex, P5 is defined to be toward the  $\text{NH}_3$  (3,3) peak and P6 coincides with the peaks of  $\text{NH}_3$  (1,1), (2,2), and (6,6). Finally, P7 and P8 are defined to be on the respective peaks of clumps E and F. The positions of P1 to P8 are displayed in Fig. 6 and their line properties are listed in Table 2. Ammonia spectra of those positions are shown in Fig. 7. In the same figure, we also show CO spectra for comparison. The individual ammonia linewidths and brightness peaks toward the SW do not differ significantly from those toward the NE region despite the larger total, spatially integrated flux of the SW region (see Sect. 3.2, Fig. 3, and Table 1). This implies that there is more extended emission toward the SW than the NE. The CO spectra for P4 to P7 are very broad and some subcomponents extend well to the other side of the systemic velocity of NGC 253. This is similar to the velocity structure of CS (Peng et al. 1996) but, as noted above, cannot be extracted from our ammonia data.

$\text{NH}_3$  (1,1), (2,2), and (6,6) absorption is seen toward the 1.2 cm continuum source at P4. If a similar absorption feature for  $\text{NH}_3$  (3,3) exists, it is blended with emission of this line. The reason for the  $\text{NH}_3$  (3,3) emission at P4 may be obvious from the contours of the pV diagram in Fig. 5, where a faint, central  $\text{NH}_3$  (3,3) feature extends from the systemic velocity of NGC 253 to  $\sim 400$  km s $^{-1}$ . A similar feature is seen in OH (Turner 1985) and SiO (García-Burillo et al. 2000). García-Burillo et al. (2000) speculate that this may be evidence for molecular outflows from the starburst. Our elongated beam toward the possible outflow direction, however, inhibits the identification of a spatial offset of the faint plume along the minor axis of NGC 253. Therefore, we cannot exclude other line broadening mechanisms. The reason why we only observe this feature in  $\text{NH}_3$  (3,3) but not in the other ammonia transitions may be the peculiar distribution of energy levels in ortho- $\text{NH}_3$ , which allow the line to be a maser under certain circumstances. Walmsley & Ungerechts (1983)

show that at  $\text{H}_2$  volume densities of  $10^{4-5} \text{ cm}^{-3}$  the populations of the two inversion levels can be inverted (see also Schilke 1989). Such masers are known to exist in a few prominent Galactic star forming regions, such as DR 21 and W 33 (Guilloteau et al. 1983; Wilson & Mauersberger 1990; Wilson et al. 1995). Apparently, these masers are unsaturated, requiring seed photons from the background continuum of the associated  $\text{H II}$  regions. It may therefore not be accidental that the  $\text{NH}_3$  (3,3) emission feature, accompanied by (1,1), (2,2), and (6,6) absorption features, is observed toward the nuclear continuum of NGC 253. Toward the same central region of NGC 253 OH and  $\text{H}_2\text{O}$  masers are already known to exist (Frayer, Seaquist, & Frail 1998; Henkel et al. 2004). Thus,  $\text{NH}_3$  may represent the third molecular species known to exhibit maser emission in the central environment of NGC 253. If confirmed, it would be the first extragalactic  $\text{NH}_3$  maser ever detected ( $\text{NH}_3$  would then be the sixth molecule showing maser emission in extragalactic objects; for  $\text{OH}$ ,  $\text{H}_2\text{O}$ ,  $\text{CH}$ ,  $\text{H}_2\text{CO}$ , and  $\text{SiO}$ , see Welischew 1971; Churchwell et al. 1977; Whiteoak, Gardner, & Hoglund 1980; Baan, Guesten, & Haschick 1986; van Loon et al. 1996).

### 4.3. Rotational Temperatures

As indicated in the introduction, ammonia can be used to determine rotational temperatures of the dense molecular gas. To derive rotational temperatures from ammonia in emission, populations of more than one metastable ( $J = K$ ) inversion doublet have to be determined. Assuming optically thin line emission, the column densities of their upper states  $N_u$  can be derived via:

$$N_u(J, K) = \frac{7.77 \times 10^{13}}{\nu} \frac{J(J+1)}{K^2} \int T_{\text{mb}} \, dv \quad (1)$$

(Henkel et al. 2000) where  $N_u$  is given in units of  $\text{cm}^{-2}$ , the frequency  $\nu$  in GHz, the main beam brightness temperature  $T_{\text{mb}}$  in K, and the velocity  $v$  in  $\text{km s}^{-1}$ .

For ammonia in absorption, the column densities of the different populations cannot be determined without the knowledge of the excitation temperature  $T_{\text{ex}}$  across an individual inversion doublet. The following equation applies:

$$\frac{N(J, K)}{T_{\text{ex}}} = 1.61 \times 10^{14} \frac{J(J+1)}{K^2 \nu} \tau \Delta v_{1/2} \quad (2)$$

(Hüttemeister et al. 1995) with  $\Delta v_{1/2}$  denoting the FWHM of the line in  $\text{km s}^{-1}$ . The optical depth  $\tau$  is derived from the brightness temperatures of the line  $T_L$  and the continuum  $T_C$  by

$$\tau = -\ln \left( 1 - \frac{|T_L|}{T_C} \right). \quad (3)$$

From the different  $N_u$  of the metastable ( $J = K$ ) inversion lines, the rotational temperatures  $T_{JJ'}$  can be derived using

$$\frac{N_u(J', J')}{N_u(J, J)} = \frac{g_{\text{op}}(J')}{g_{\text{op}}(J)} \frac{2J' + 1}{2J + 1} \exp \left( \frac{-\Delta E}{T_{JJ'}} \right) \quad (4)$$

(corrected version of the equation given in Henkel et al. 2000).  $\Delta E$  is the energy difference between the  $\text{NH}_3(J', J')$  and the  $\text{NH}_3(J, J)$  levels in K [41.2 K between  $\text{NH}_3$  (1,1) and (2,2), and 284.4 K between  $\text{NH}_3$  (3,3) and (6,6)],  $g_{\text{op}}$  are the statistical weights given as  $g_{\text{op}} = 1$  for para-ammonia [ $\text{NH}_3$  (1,1) and (2,2)] and  $g_{\text{op}} = 2$  for ortho-ammonia [ $\text{NH}_3$  (3,3) and (6,6)]. This equation is applicable for emission and is also valid for absorption lines when it is assumed that both transitions have the same  $T_{\text{ex}}$ . Our LVG analysis (see below) shows that excitation temperatures of  $\text{NH}_3$  (1,1) and (2,2) are indeed very similar, which is not necessarily the case for  $\text{NH}_3$  (3,3) and (6,6).

In Table 3 the column densities of the upper levels ( $N[J, K]/T_{\text{ex}}$  for P4) and the rotational temperatures of the ammonia spectra at positions P1 to P8 are listed. The column densities of the para- $\text{NH}_3$ (1,1) and ortho- $\text{NH}_3$ (3,3) transitions may differ by up to a factor of two with a slight trend for  $N_u(1,1)$  to be larger. In spite of their higher statistical weights, the (2,2) and (6,6) levels are less populated than the lower counterparts of the respective ammonia variant. The rotational temperatures  $T_{12}$  (using the para-ammonia [1,1] and [2,2] inversion lines) are in the range of 35 – 65 K for the emission components and 88 K (statistical  $1\sigma$  error including calibration uncertainties:  $\sim 2$  K) for the absorption component. The rotational temperatures of ortho- $\text{NH}_3$  ( $T_{36}$ ; using  $\text{NH}_3$  [3,3] and [6,6]) are in the range of  $\sim 105$  – 140 K (see Table 3). In Fig. 8 we compare Boltzmann plots (also referred to as rotational diagrams) of our analysis with those from the single dish observations presented by M03 and T02. Since the NE and SW component are clearly discernible in velocity space, the different regions can be separated in the single-dish data. Because parts of the analyses in T02 and M03 are different from ours (e.g., M03 fit a single rotation temperature using data of all transitions) we extracted the brightness temperatures from their papers and followed our methods described above. In the Boltzmann plot, the slopes between different inversion transitions represent rotational temperatures with steep slopes corresponding to low rotational temperatures. We find that our column densities are very similar to those of M03 and exceed those of T02. T02 did not observe the  $\text{NH}_3$ (6,6) line and could therefore not derive  $T_{36}$ . Their  $T_{12}$  is lower than ours for both the SW and the NE components but confirm

the trend of higher temperatures toward the SW. The temperature distribution is reversed in the analysis of M03. Using HCN and CO data, Paglione et al. (2004) independently find higher temperatures toward the SW than toward the NE which agrees with our analysis and that of T02.

#### 4.4. LVG Analysis

##### 4.4.1. LVG Models

As shown by Walmsley & Ungerechts (1983) and Danby et al. (1988), kinetic temperatures and  $T_{12}$  and  $T_{36}$  rotational temperatures of  $\text{NH}_3$  are similar up to 20 and 60 K, respectively. Our rotational temperatures, however, are above those values and therefore the kinetic temperatures exceed the rotational temperatures considerably. To derive kinetic temperatures, we applied our LVG models using collisional rate coefficients and cross sections of Danby et al. (1988) (see also Schöier et al. 2005). The LVG models predict column densities for all levels which depend on the kinetic temperature, the  $\text{H}_2$  volume density, a velocity gradient, and the temperature of the cosmic microwave background (CMB). For our calculations we set the CMB temperature to 2.73 K and the velocity gradient to  $dv/dr = 1 \text{ km s}^{-1} \text{ pc}^{-1}$ . In the case of optically thin lines, which is considered here,  $\text{NH}_3$  column densities scale linearly with  $\text{NH}_3$  abundances. In Fig. 9 the column densities in the upper (1,1) to (6,6) levels are shown for different models using an ortho-to-para (*o/p*) ammonia ratio of unity. The densities ( $n_u^{\text{lvg}}$ ) are displayed in the natural units of the LVG code which can be converted to measured column densities of the upper levels  $N_u$  via

$$N = [n^{\text{lvg}} / (dv/dr)] \times 3.08 \times 10^{18} \times \Delta v_{1/2}; \quad (5)$$

$N$  given in  $\text{cm}^{-2}$ ,  $n^{\text{lvg}}$  in  $\text{cm}^{-3}$ ,  $\Delta v_{1/2}$  in  $\text{km s}^{-1}$ , and the velocity gradient  $dv/dr$  in  $\text{km s}^{-1} \text{ pc}^{-1}$ . As shown in Fig. 9(a), the computed ammonia column densities of the metastable lines are virtually independent of the  $\text{H}_2$  density. Most complex molecules in interstellar space were found at densities  $10^4 \text{ cm}^{-3} \lesssim n_{\text{H}_2} \lesssim 10^7 \text{ cm}^{-3}$  and we expect that the densities of the environment from which the ammonia is emitted in NGC 253 are within that range. For all further calculations, we therefore fixed  $n_{\text{H}_2}$  to a value of  $10^5 \text{ cm}^{-3}$ .

Temperature dependencies are shown in Figs. 9(b) and (c). The fits are most conclusive at low ( $\lesssim 50$  K) kinetic temperatures where population differences relative to  $\text{NH}_3(1,1)$  column densities are most sensitive to changes in  $T_{\text{kin}}$ . At higher temperatures, the ratios between the weighted column densities become more and more constant and the curves in the

Boltzmann plot (Fig. 9[c]) are spaced by smaller intervals. As expected, the slopes between the data points at a given kinetic temperature are steeper than those for  $T_{\text{rot}} = T_{\text{kin}}$ . In other words, rotational temperatures underestimate kinetic temperatures (see above). The most distinctive changes in slope of  $T_{\text{rot}}$  are predicted to be at the  $\text{NH}_3(3,3)$  transition and are most prominent at kinetic temperatures  $\gtrsim 50$  K. Without using radiative transfer codes, the closest match between  $T_{\text{rot}}$  and  $T_{\text{kin}}$  is therefore provided by all transitions at  $T_{\text{kin}} \lesssim 50$  K, and by the highest states including (3,3) at  $T_{\text{kin}} \gtrsim 50$  K.

#### 4.4.2. Kinetic Temperatures

We attempted to fit the LVG models to the measured ammonia transitions at the different positions toward NGC 253. To do so, we applied one- and two-temperature models to the data. The second temperatures in the latter models, however, are usually very similar to the first temperatures and are therefore not required. One-temperature fits are shown in Fig. 10 for the NE and SW regions. In general the one-temperature fits with  $o/p = 1$  were underestimating the  $\text{NH}_3(3,3)$  column densities but provide reasonable fits to the SW spectra. Still, the fits are substantially improved when the  $o/p$  ratio is treated as a free parameter. In that case, the data and the models are virtually indistinguishable. The results of the fits are listed in Table 4. We estimate the errors of the fits including the free  $o/p$  parameter to  $\sim 20\%$ .

The resulting kinetic temperatures are  $\sim 200$  K in the SW and  $\sim 140$  K in the NE. Those values are in agreement with the analysis of Rigopoulou et al. (2002). They use infrared ISO–SWS data to determine  $\text{H}_2$  excitation temperatures of the molecular gas. In addition to two phases with much higher temperatures, they detect  $\text{H}_2$  at a temperature of  $\sim 200$  K. Based on *Spitzer* and near-infrared data, Devost et al. (2004) and Pak et al. (2004) show that toward the SW the strengths of the  $\text{H}_2(0-0)\text{S}(1)$  and  $(1-0)\text{S}(1)$  lines are larger than those toward the NE, indicating a larger amount of warm gas toward the SW. This result corroborates our derived temperature difference between the NE and SW regions. Temperatures in the observed range may be explained by shock heating as proposed for the central Galactic region (e.g., Flower, Pineau des Forets, & Walmsley 1995; Hüttemeister et al. 1995; Martín-Pintado et al. 2001) and also for NGC 253 itself and other starburst galaxies (e.g., García-Burillo et al. 2000; Devost et al. 2004; Pak et al. 2004). Other processes, such as ion-slip or cosmic ray heating, as well as dynamic heating by the bar may also have an influence on the temperature of the dense gas. The kinetic temperature as a function of galactocentric distance are displayed for the individual positions P1 to P8 and the entire NE and SW regions in Fig. 11(a). Whereas the temperature variations within the SW and NE

regions are not significant, the temperature difference between the two sides of the nucleus is notable. Some additional heating may therefore have occurred in the SW of NGC 253. For possible mechanisms, see the end of Sect. 4.4.4 and Sect. 4.5.

#### 4.4.3. The Ortho-to-Para Ammonia Ratio

The  $o/p$  ratio depends on the energy that is transferred to the  $\text{NH}_3$  molecule during its formation and equilibration (see Sect. 1). At low energies, only the lowest (0,0) state can be populated which belongs to ortho-ammonia. This results in an increase of the  $o/p$  ratio. Due to the very slow decay of the metastable inversion states, the  $o/p$  ratio is not significantly altered once the formation and equilibration processes are completed (see, e.g., Cheung et al. 1969; Ho & Townes 1983). As shown in T02, the theoretical  $o/p$  ratio is about unity at formation temperatures above  $\sim 30\text{ K}$  and  $o/p$  rises steeply at lower temperatures. The  $o/p$  ratio therefore offers an archaeological view on the initial conditions of the molecular gas during its formation.

We derive  $o/p$  ratios of  $\sim 1$  in the SW region, which would correspond to an  $\text{NH}_3$  formation temperature above  $\sim 30\text{ K}$  (cf. fig. 3 in T02). In the NE region  $o/p$  is with  $\sim 1.5 - 2$  significantly larger (Table 4, Fig. 11b). Such  $o/p$  ratios suggest lower ammonia formation temperatures of  $\sim 15 - 20\text{ K}$  toward the NE. This result is in agreement with the derived kinetic temperatures which are also higher in the SW region.

Since LVG models are rarely applied when analyzing extragalactic  $\text{NH}_3$  emission,  $o/p$  ratios are usually calculated in a different way making use of deviations from a constant  $T_{12}$  rotational temperature model (a single line in the Boltzmann plot; see, e.g., T02; Takano et al. 2000). As shown in Fig. 10 this approach may provide reasonable  $o/p$  values when adjusting the ortho- $\text{NH}_3(3,3)$  column densities to the extrapolated (para- $\text{NH}_3$ )  $T_{12}$  temperature (note that the kinetic temperatures of the LVG models with a fixed  $o/p = 1$  and a free  $o/p$  are similar, Table 4). This approach fails, however, when the ortho- $\text{NH}_3(6,6)$  column densities are scaled to match the extrapolated  $T_{12}$ . The best method without the application of radiative transfer models is to adjust para- $\text{NH}_3(4,4)$  or (5,5) weighted column densities to  $T_{36}$  (see Fig. 9[c]).

#### 4.4.4. Ammonia Column Densities, Abundances, and Masses

Total ammonia column densities are calculated by adding up the column densities derived for the populations of the individual rotational levels. A rough estimate is given by

the sum of the *observed* levels  $N_{1236}(\text{NH}_3) \equiv 2 \sum_{J=1,2,3,6} N_u(J, J)$  (Table 3). The factor of 2 has been introduced to accommodate the populations of the lower inversion levels (which contribute equally to the column densities due to the low energy difference between upper and lower states of  $\sim 1$  K). A map of the spatial  $N_{1236}(\text{NH}_3)$  distribution is shown in Fig. 6. The column densities for the individual clumps are in the range of  $\sim 30 - 50 \times 10^{13} \text{ cm}^{-2}$  (Table 3). Averaged over the entire NE and SW regions, however, the  $\text{NH}_3$  column densities drop to  $\sim 10 \times 10^{13} \text{ cm}^{-2}$  toward the NE and to  $\sim 13 \times 10^{13} \text{ cm}^{-2}$  toward the SW, due to the inclusion of large-scale diffuse emission between the individual complexes A to F. Therefore, both regions within NGC 253 exhibit similar averaged  $\text{NH}_3$  columns.

Using only the observed values, however, underestimates the true column densities due to the contributions of the other ammonia levels. The LVG models predict that collisional excitation of the non-metastable levels leads to populations about three orders of magnitudes below those of metastable levels. The column densities of the non-metastable levels may, however, increase substantially by infrared pumping (e.g., Mauersberger et al. 1985) which is not incorporated in our code. Among the metastable levels, the most prominent are the  $\text{NH}_3(0,0)$ , (4,4) and (5,5) levels. Adding up all the levels involved in our LVG code (up to the metastable [6,6] levels) the total  $\text{NH}_3$  column densities are  $\sim 1.5 - 2.5$  times larger than  $N_{1236}$ , corresponding to column densities of  $6 - 11 \times 10^{14} \text{ cm}^{-2}$  for the individual clumps (Table 4). The column densities averaged over the NE and SW regions are about 2–3 times lower than the column densities in the peaks.

Ammonia masses within the NE and SW regions are derived to  $\sim 9$  and  $\sim 10 \text{ M}_\odot$ , respectively, and are therefore comparable. They add up to a total ammonia mass of  $\sim 20 \text{ M}_\odot$  within the central 2' of NGC 253 (see Table 4).

$\text{NH}_3$  abundances are computed relative to the column densities of  $\text{H}_2$ . The latter are derived using the CO data (see Sect. 3.2) with a CO-to- $\text{H}_2$  conversion factor of  $X_{\text{CO}} = 5 \times 10^{19} \text{ cm}^{-2} (\text{K km s}^{-1})^{-1}$ . This value was determined for ultraluminous far infrared galaxies by Downes & Solomon (1998) and is widely used for starburst galaxies in the literature. For NGC 253 itself, Mauersberger et al. (1996) suggest a similar value of  $X_{\text{CO}} \sim 3 \times 10^{19} \text{ cm}^{-2} (\text{K km s}^{-1})^{-1}$  based on single-dish CO data. Note, however, that  $X_{\text{CO}}$  is not necessarily constant over the entire starburst. Using multi-transition, interferometric CO observations toward the starburst galaxy M 82, Weiß et al. (2001b) showed that  $X_{\text{CO}}$  varies in the range of 3 to  $10 \times 10^{19} \text{ cm}^{-2} (\text{K km s}^{-1})^{-1}$  along the major axis.

The ammonia abundances derived toward the different positions in NGC 253 are listed in Table 4 and are shown as a function of galactocentric distance in Fig. 11(d). We also produced a map of the ammonia abundances relative to  $\text{H}_2$  (based on  $N_{1236}[\text{NH}_3]$ ; see the caveats above) which is shown in Fig. 12. The fractional ammonia abundances vary in the

range of  $\sim 25 - 45 \times 10^{-9}$ . The overall abundances are only slightly larger than those derived for NGC 253 by M03 ( $\sim 20 \times 10^{-9}$ ). Typical ammonia abundances of Galactic molecular clouds are with  $\sim 30 \times 10^{-9}$  in the same range (e.g., Irvine et al. 1987; Walmsley & Schilke 1993). Note that toward the Galactic Center, the ammonia abundances are at least as large as toward Galactic interstellar clouds (e.g., Flower, Pineau des Forets, & Walmsley 1995; Goicoechea et al. 2004).

An  $\text{NH}_3$  abundance gradient is visible along the SW complex with minimal values near the starburst center (Figs. 11(d) and 12; note that the abundance between P6 and P5, approaching the center from the NE, is also decreasing). The abundance toward the SW varies from  $\sim 2.5 \times 10^{-8}$  to  $\sim 3.5 \times 10^{-8}$  at distances of  $\sim 40$  pc and  $\sim 250$  pc from the nucleus, respectively. A similar gradient has been found for M 82 by Weiß et al. (2001a), varying from  $\sim 2 \times 10^{-10}$  close to the starburst center to  $\sim 6 \times 10^{-10}$  at larger radii. Those values, however, are about two orders of magnitude lower than the ammonia abundances in NGC 253. The abundance gradient may be explained by the destruction of  $\text{NH}_3$  by photo-dissociation near the starburst similar to what has been proposed for M 82 by Weiß et al. (2001a). Whereas the entire ammonia abundance is raised by liberating  $\text{NH}_3$  from grains by shocks (see also Sect. 4.4.2), close to the nucleus of NGC 253 the molecules may be destroyed by photons with energies above  $\sim 4.1$  eV, the dissociation energy of  $\text{NH}_3$  (Suto & Lee 1983). *Spitzer* data of [Ne II] and [Ne III] toward NGC 253 show that most of the ionizing flux is produced close to the starburst center, probably with a slight offset toward the SW, and decreases with galactocentric radius (Devost et al. 2004, note that radiation hardens with increasing radius but, due to the low dissociation threshold of ammonia, this is only a second order effect to the destruction of  $\text{NH}_3$ ). This can potentially explain the  $\text{NH}_3$  abundance gradient. The molecular gas, however, may be shielded against the UV photons by dust. A 2MASS  $J - K$  color map (Fig. 12[b]) shows that there is only little radial variation of the optical and infrared absorption caused by dust along the molecular condensation toward the SW. Shielding should therefore be a relatively constant parameter and the ammonia abundance gradient remains a function of ionizing photons emerging from the starburst center.

The suggestion that the SW is more affected by photo-dissociation than the NE may also be corroborated by infrared observations toward the central region of NGC 253. With respect to the nucleus (position (J2000):  $\alpha=00^h 47^m 33\rlap{.}^s 174$ ,  $\delta=-25^\circ 17' 17\rlap{.}'' 08$ ; Ulvestad & Antonucci 1997, based on VLA 1.3 cm data), the infrared peak is shifted by  $2''$ - $3''$  toward the SW (Keto et al. 1993; Sams et al. 1994; Böker et al. 1998). While this corresponds only to a fraction of the ATCA beam at 1.2 cm, it may nevertheless indicate that the intensity of SF is increased toward the SW of the nucleus of NGC 253, which heats the molecular gas as probed by  $\text{NH}_3$ , and may dissociate a large fraction of the ammonia molecules (see also Sect. 4.5).

#### 4.5. An Expanding Shell in the Dense Gas

Toward the northern end of the ammonia emission in the SW region, pV cuts of the data cubes reveal a feature resembling an expanding shell that is visible in all inversion lines (see Fig. 13). Given the elliptic beam of the radio data, the position of this feature is somewhat uncertain. However, the largest contrast between the rim and the center of this shell is found at a location coincident with an X-ray point source detected in ACIS-S3 images taken with the *Chandra X-ray Observatory* (obs. id 969) at  $\alpha_{(J2000)} = 00^h47^m32^s.0$ ,  $\delta_{(J2000)} = -25^\circ17'21''.4$ . The X-ray spectrum of this source is shown in Fig. 13(c). We fitted an APEC collisional equilibrium plasma (Smith et al. 2001) with solar metallicity as well as a power law model to this source (for the data reduction technique see Ott, Walter, & Brinks 2005). Both models provide good fits to the data. The APEC fit results in an absorbing column density of  $N_{\text{H}} = (2.8 \pm 0.3) \times 10^{22} \text{ cm}^{-2}$  (excluding Galactic H I emission), a temperature of  $T_{\text{plasma}} = (3.6 \pm 0.7) \times 10^7 \text{ K}$ , a flux of  $F = (1.9 \pm 0.7) \times 10^{13} \text{ erg cm}^{-2} \text{ s}^{-1}$ , and an unabsorbed X-ray luminosity (0.3–6.0 keV)  $L_X = (4.7 \pm 0.7) \times 10^{38} \text{ erg s}^{-1}$ . The power law fit yields  $N_{\text{H}} = (2.9 \pm 0.3) \times 10^{22} \text{ cm}^{-2}$ , a photon index of  $\Gamma = 2.3 \pm 0.1$ ,  $F = (2.2 \pm 0.9) \times 10^{-13} \text{ erg cm}^{-2} \text{ s}^{-1}$ , and  $L_X = (10.3 \pm 2.1) \times 10^{38} \text{ erg s}^{-1}$ . In Fig. 13 we show the APEC fit overlaid on the X-ray spectrum; the power law fit looks very similar. The X-ray absorbing column density can be compared to that of molecular hydrogen. From the CO data (resolution used here:  $5''.88 \times 2''.87$ ) we derive a luminosity of  $\sim 1.1 \times 10^3 \text{ K km s}^{-1}$  which translates into a proton column density of  $5.5 \times 10^{22} \text{ cm}^{-2}$ , using a CO-to-H<sub>2</sub> conversion factor of  $5 \times 10^{19} \text{ cm}^{-2} (\text{K km s}^{-1})^{-1}$  (see Sect. 4.4.4). This value is about twice as large as that derived by X-ray absorption, which suggests that the X-ray point source is embedded in the molecular material.

As shown in Fig. 13(b), the shell is centered at a LSR velocity of  $\sim 310 \text{ km s}^{-1}$  and expands at  $v_{\text{exp}} \sim 30 \text{ km s}^{-1}$ . Its radius is  $\sim 3''$  which corresponds to  $\sim 40 \text{ pc}$  at the distance to NGC 253. The dynamical age of the shell is therefore  $\sim 1.3 \text{ Myr}$ . Using the shell radius and the proton column density derived above, we estimate the mass of the shell to  $\sim 8 \times 10^6 \text{ M}_\odot$  and its kinetic energy to  $\sim 7 \times 10^{52} \text{ erg}$ . This figure is about two (power law model) to four (APEC) times larger than the energy input of the X-ray source over the lifetime of the shell. Using the STARBURST99 models (Leitherer et al. 1999) to derive the starburst properties (see Ott, Martin, & Walter 2003, for details), and assuming that the X-ray luminosity is due to thermalized mechanical luminosity, the total energy input matches that of a stellar cluster with a mass of  $\sim 10^5 \text{ M}_\odot$  (assuming an instantaneous starburst, a solar metallicity, and a Salpeter IMF with a lower and upper mass cutoff of 1 and  $100 \text{ M}_\odot$ , respectively) which must be highly obscured by the dust visible in the 2MASS  $J - K$  map (see Fig. 12). The I-band surface brightness at the position of the cluster candidate (as visible in an uncalibrated F814W HST/WFPC2 image; proposal ID: 5211) is slightly enhanced (factor of  $\sim 1.2$ ) as

compared to its surroundings. A mass of  $\sim 10^5 M_{\odot}$  is typical for globular clusters in the Galaxy (e.g., Mandushev et al. 1991) and would also fit the distribution of globular clusters in the halo of NGC 253 (Beasley & Sharples 2000). Note that a young globular cluster candidate of similar mass has been found in NGC 253 toward the SW infrared peak (Watson et al. 1996; Keto et al. 1999).

Ulvestad (2000) reports a radio continuum source (2 cm VLA observations) which is located  $\sim 2''$  toward the east of the X-ray point source which may be related to the globular cluster candidate. Within the dynamical timescale of the shell, massive stars could not have exploded as supernovae. The energy which drives the shell of dense gas must therefore be provided by massive stellar winds which shock their ambient medium and thermalize some of it to coronal temperatures.

For the shell the rotational temperature of the dense gas was estimated separately using the ammonia observations. Over the area of the shell, we derive  $T_{12,\text{shell}} = (87 \pm 12)$  K and  $T_{36,\text{shell}} = (266 \pm 40)$  K, which is well a factor of  $\sim 2$  above the mean rotational temperatures averaged over the ammonia emission in the SW and which converts to extremely high kinetic temperatures. This may indicate that the energetic input of the super cluster candidate has heated the surrounding molecular medium. As mentioned in Sect. 4.4.2, Devost et al. (2004) and Pak et al. (2004) detect some higher  $H_2(0-0)$  S(1) and (1-0) S(1) emission toward the SW region as compared to the NE which coincides with the location of the shell. The shock produced by the central source and the subsequent expansion of the shell may therefore have excited the molecular hydrogen and heated the surroundings. This can potentially explain the higher kinetic temperatures in the SW region as derived in Sect. 4.4.2. Unlike the starburst near the center of NGC 253 (see the end of Sect. 4.4.4), the stellar cluster may be too young to effectively photo-dissociate its environment.

## 5. Summary

In this paper we present the first interferometric ammonia observations toward NGC 253, one of the most nearby starburst galaxies. Our analysis of the ATCA data reveal the following:

1. Using the unresolved 1.2 cm continuum emission toward the starburst nucleus in NGC 253 (flux:  $520 \pm 52$  mJy), we derive a SFR of  $\sim 2.8 M_{\odot} \text{ yr}^{-1}$  which agrees well with earlier FIR estimates.
2. Ammonia is detected in NGC 253 up to a radius of  $\sim 250$  pc toward the SW and up to  $\sim 200$  pc toward the NE of the nuclear starburst in NGC 253. Three individual

molecular clumps are identified within those regions on either side of the nucleus. The ammonia components are found at velocities of up to  $\sim 150 \text{ km s}^{-1}$  relative to the systemic velocity of NGC 253. Very close to the starburst the north–eastern, innermost  $\text{NH}_3$  (3,3) emission peak is closer to the nucleus than the peaks of the other ammonia lines.

3. The line shapes and the morphology of ammonia are similar to those of other molecular species such as CO, CS, SiO, and  $\text{H}^{13}\text{CO}^+$ . However, some components traced by those molecules were not detected in  $\text{NH}_3$  which can partly be attributed to the S/N of our observations.
4. Toward the nuclear continuum source we observe  $\text{NH}_3$ (1,1), (2,2), and (6,6) in absorption but  $\text{NH}_3$ (3,3) in emission. This might indicate the presence of an ammonia maser.
5. From our large velocity gradient models we find that for each position toward NGC 253 a one-temperature gas with a non-uniform ortho–to–para (*o/p*) ammonia abundance delivers excellent agreement with the data, despite of different rotational temperatures  $T_{12}$  and  $T_{36}$ . The kinetic temperatures in the NE region hover around 140 K. In the SW region they are with about 200 K significantly higher.
6. Whereas the *o/p* abundance ratio is  $\sim 1$  toward the SW, we derive *o/p*  $\sim 1.5 – 2.5$  toward the NE, with the larger values close to the starburst center. Such *o/p* ratios correspond to  $\text{NH}_3$  formation temperatures of  $\gtrsim 30$  and  $\sim 15 – 20$  K toward the SW and NE, respectively. Thus, the ammonia formation and kinetic temperatures show the same trend, being warmer in the SW than in the NE.
7. Total ammonia column densities are  $\sim 3 \times 10^{14} \text{ cm}^{-2}$  toward the NE and  $\sim 2 \times 10^{14} \text{ cm}^{-2}$  toward the SW. For the individual clumps we derive column densities in the range of  $\sim 6 – 11 \times 10^{14} \text{ cm}^{-2}$ . The total ammonia mass adds up to  $\sim 20 \text{ M}_\odot$  with about half of the mass toward either side of the starforming nucleus. In NGC 253, ammonia abundances toward the most prominent molecular complexes are  $\sim 2.5 – 4.5 \times 10^{-8}$  with respect to  $\text{H}_2$ . Decreasing abundances are measured in the SW complex toward the starburst center. At the position of the lowest  $\text{NH}_3$  abundance, prominent dust features are visible in near-infrared 2MASS color images. As the starburst in NGC 253 is slightly shifted toward the SW, the resulting UV radiation may photo-dissociate the fragile ammonia molecules predominantly in this region.
8. An expanding shell feature is detected within the SW molecular complex. The shell coincides with a bright X-ray point source. The absorbing column density of the X-ray

source as compared to the total molecular column reveals that this source is likely located inside the shell. The shell has a dynamical age of  $\sim 1.3$  Myr and a kinetic energy of  $\sim 7 \times 10^{52}$  erg. This corresponds to the energy input of a stellar cluster with a mass of  $\sim 10^5 M_\odot$ . An optical identification of this cluster is very difficult due to high visual obscuration. At the position of the shell, the rotational temperature of ammonia is enhanced by a factor of  $\sim 2$  over the mean of the SW region, coincident with a local maximum of H<sub>2</sub> excitation temperatures. This supports the scenario that large amounts of energy are injected into the dense gas.

Our study demonstrates the power of interferometric multi-transition ammonia observations to constrain in detail the physical conditions of the various phases of molecular gas in starburst environments. The application of radiative transfer models to the data allows us to determine the conditions with better accuracy than previously possible. Studies of other nearby actively star forming galaxies will be needed to find out whether NGC 253 provides a typical environment and may therefore be used as a prototype for comparisons with more distant, even more vigorously violently star forming objects.

The Australia Telescope Compact Array is part of the Australia Telescope which is funded by the Commonwealth of Australia for operation as a National Facility managed by CSIRO. We thank Michael Dahlem for the provision of the CO data. We are also grateful to Rainer Mauersberger and the referee for their comments on the manuscript. C.H. thanks for support provided by ATNF during his time spent at ATNF and ATCA. This research has made use of the NASA/IPAC Extragalactic Database (NED), which is maintained by the Jet Propulsion Laboratory, Caltech, under contract with the National Aeronautics and Space Administration (NASA), NASA’s Astrophysical Data System Abstract Service (ADS), NASA’s SkyView and the NASA/IPAC Infrared Science Archive, which is operated by the Jet Propulsion Laboratory, California Institute of Technology, under contract with the National Aeronautics and Space Administration.

Facilities: ATCA, OVRO, Chandra, HST

## REFERENCES

- Baan, W. A., Guesten, R., & Haschick, A. D. 1986, ApJ, 305, 830  
Bayet, E., Gerin, M., Phillips, T. G., & Contursi, A. 2004, A&A, 427, 45  
Beasley, M. A., & Sharples, R. M. 2000, MNRAS, 311, 673

- Böker, T., Krabbe, A., & Storey, J. W. V. 1998, *ApJ*, 498, L115
- Bradford, C. M., Nikola, T., Stacey, G. J., Bolatto, A. D., Jackson, J. M., Savage, M. L., Davidson, J. A., & Higdon, S. J. 2003, *ApJ*, 586, 891
- Brinchmann, J., Charlot, S., White, S. D. M., Tremonti, C., Kauffmann, G., Heckman, T., & Brinkmann, J. 2004, *MNRAS*, 351, 1151
- Cheung, A. C., Rank, D. M., Townes, C. H., Knowles, S. H., & Sullivan, W. T. 1969, *ApJ*, 157, L13
- Churchwell, E., Witzel, A., Huchtmeier, W., Pauliny-Toth, I., Roland, J., & Sieber, W. 1977, *A&A*, 54, 969
- Condon, J. J. 1992, *ARA&A*, 30, 575
- Danby, G., Flower, D. R., Valiron, P., Schilke, P., & Walmsley, C. M. 1988, *MNRAS*, 235, 229
- Das, M., Anantharamaiah, K. R., & Yun, M. S. 2001, *ApJ*, 549, 896
- Devost, D., et al. 2004, *ApJS*, 154, 242
- Downes, D. & Solomon, P. M. 1998, *ApJ*, 507, 615
- Engelbracht, C. W., Rieke, M. J., Rieke, G. H., Kelly, D. M., & Achtermann, J. M. 1998, *ApJ*, 505, 639
- Flower, D. R., Pineau des Forets, G., & Walmsley, C. M. 1995, *A&A*, 294, 815
- Forbes, D. A., Polehampton, E., Stevens, I. R., Brodie, J. P., & Ward, M. J. 2000, *MNRAS*, 312, 689
- Frayer, D. T., Seaquist, E. R., & Frail, D. A. 1998, *AJ*, 115, 559
- Gao, Y. & Solomon, P. M. 2004, *ApJS*, 152, 63
- García-Burillo, S., Martín-Pintado, J., Fuente, A., & Neri, R. 2000, *A&A*, 355, 499
- Geldzahler, B. J. & Witzel, A. 1981, *AJ*, 86, 1306
- Goicoechea, J. R., Rodríguez-Fernández, N. J., & Cernicharo, J. 2004, *ApJ*, 600, 214
- Gooch, R. 1996, *ASP Conf. Ser.* 101: *Astronomical Data Analysis Software and Systems V*, 5, 80

- Guilloteau, S., Wilson, T. L., Batrla, W., Martin, R. N., & Pauls, T. A. 1983, A&A, 124, 322
- Haarsma, D. B., Partridge, R. B., Windhorst, R. A., & Richards, E. A. 2000, ApJ, 544, 641
- Henkel, C., Tarchi, A., Menten, K. M., & Peck, A. B. 2004, A&A, 414, 117
- Henkel, C., Mauersberger, R., Peck, A. B., Falcke, H., & Hagiwara, Y. 2000, A&A, 361, L45
- Ho, P. T. P. & Townes, C. H. 1983, ARA&A, 21, 239
- Ho, P. T. P., Martin, R. N., Turner, J. L., & Jackson, J. M. 1990, ApJ, 355, L19
- Houghton, S., Whiteoak, J. B., Koribalski, B., Booth, R., Wiklind, T., & Wielebinski, R. 1997, A&A, 325, 923
- Hüttemeister, S., Wilson, T. L., Mauersberger, R., Lemme, C., Dahmen, G., & Henkel, C. 1995, A&A, 294, 667
- Irvine, W. M., Goldsmith, P. F., & Hjalmarson, A. 1987, ASSL Vol. 134: Interstellar Processes, 561
- Jackson, J. M., Paglione, T. A. D., Carlstrom, J. E., & Rieu, N. 1995, ApJ, 438, 695
- Jarrett, T. H., Chester, T., Cutri, R., Schneider, S. E., & Huchra, J. P. 2003, AJ, 125, 525
- Karachentsev, I. D., et al. 2003, A&A, 404, 93
- Keto, E., Ball, R., Arens, J., Jernigan, G., Meixner, M., Skinner, C., & Graham, J. 1993, ApJ, 413, L23
- Keto, E., Hora, J. L., Fazio, G. G., Hoffmann, W., & Deutsch, L. 1999, ApJ, 518, 183
- Leitherer, C., et al. 1999, ApJS, 123, 3
- Martin, R. N. & Ho, P. T. P. 1986, ApJ, 308, L7
- Martín, S., Mauersberger, R., Martín-Pintado, J., García-Burillo, S., & Henkel, C. 2003, A&A, 411, L465
- Martín-Pintado, J., Rizzo, J. R., de Vicente, P., Rodríguez-Fernández, N. J., & Fuente, A. 2001, ApJ, 548, L65
- Mauersberger, R., Wilson, T. L., Walmsley, C. M., Henkel, C., & Batrla, W. 1985, A&A, 146, 168

- Mauersberger, R., Henkel, C., Wielebinski, R., Wiklind, T., & Reuter, H.-P. 1996, A&A, 305, 421
- Mauersberger, R., Henkel, C., Weiß, A., Peck, A. B., & Hagiwara, Y. 2003, A&A, 403, 561 (M03)
- Mandushev, G., Staneva, A., & Spasova, N. 1991, A&A, 252, 94
- Ott, J., Martin, C. L., & Walter, F. 2003, ApJ, 594, 776
- Ott, J., Walter, F., & Brinks, E. 2005, MNRAS, 358, 1423
- Paglione, T. A. D., Yam, O., Tosaki, T., & Jackson, J. M. 2004, ApJ, 611, 835
- Peng, R., Zhou, S., Whiteoak, J. B., Lo, K. Y., & Sutton, E. C. 1996, ApJ, 470, 821
- Pak, S., Jaffe, D. T., Stacey, G. J., Bradford, C. M., Klumpe, E. W., & Keller, L. D. 2004, ApJ, 609, 692
- Puche, D. & Carignan, C. 1988, AJ, 95, 1025
- Radovich, M., Kahanpää, J., & Lemke, D. 2001, A&A, 377, 73
- Rigopoulou, D., Kunze, D., Lutz, D., Genzel, R., & Moorwood, A. F. M. 2002, A&A, 389, 374
- Sams, B. J., Genzel, R., Eckart, A., Tacconi-Garman, L., & Hofmann, R. 1994, ApJ, 430, L33
- Sault, R. J., Teuben, P. J., & Wright, M. C. H. 1995, ASP Conf. Ser. 77: Astronomical Data Analysis Software and Systems IV, 4, 433
- Schilke, P. 1989, Diploma Thesis, University of Bonn
- Schöier, F. L., van der Tak, F. F. S., van Dishoeck, E. F., & Black, J. H. 2005, A&A, 432, 369
- Smith, R. K., Brickhouse, N. S., Liedahl, D. A., & Raymond, J. C. 2001, ApJ, 556, L91
- Sorai, K., Nakai, N., Kuno, N., Nishiyama, K., & Hasegawa, T. 2000, PASJ, 52, 785
- Strickland, D. K., Heckman, T. M., Weaver, K. A., Hoopes, C. G., & Dahlem, M. 2002, ApJ, 568, 689
- Stutzki, J. & Winnewisser, G. 1985, A&A, 148, 254

- Suto, M. & Lee, L. C. 1983, *J. Chem. Phys.*, 78, 4515
- Takano, S., Nakai, N., Kawaguchi, K., & Takano, T. 2000, *PASJ*, 52, L67
- Takano, S., Nakai, N., & Kawaguchi, K. 2002, *PASJ*, 54, 195 (T02)
- Townes, C. H. & Schawlow, A. L. 1955, *Microwave Spectroscopy*, New York: McGraw-Hill, 1955
- Turner, B. E. 1985, *ApJ*, 299, 312
- Ulvestad, J. S. 2000, *AJ*, 120, 278
- Ulvestad, J. S. & Antonucci, R. R. J. 1997, *ApJ*, 488, 621
- Ungerechts, H., Winnewisser, G., & Walmsley, C. M. 1986, *A&A*, 157, 207
- van Loon, J. T., Zijlstra, A. A., Bujarrabal, V., & Nyman, L.-A. 1996, *A&A*, 306, L29
- Walmsley, C. M. & Ungerechts, H. 1983, *A&A*, 122, 164
- Walmsley, C. M., & Schilke, P. 1993, *Dust and Chemistry in Astronomy*, 37
- Watson, A. M., et al. 1996, *AJ*, 112, 534
- Weiß, A., Neininger, N., Henkel, C., Stutzki, J., & Klein, U. 2001a, *ApJ*, 554, L143
- Weiß, A., Neininger, N., Hüttemeister, S., & Klein, U. 2001b, *A&A*, 365, 571
- Weliachew, L. 1971, *ApJ*, 167, L47
- Whiteoak, J. B., Gardner, F. F., & Hoglund, B. 1980, *MNRAS*, 190, 17
- Whiting, A. B. 1999, *AJ*, 117, 202
- Wilson, T. L. & Mauersberger, R. 1990, *A&A*, 239, 305
- Wilson, T. L., Gaume, R. A., Johnston, K. J., & Tieftrunk, A. R. 1995, *ApJ*, 452, 693

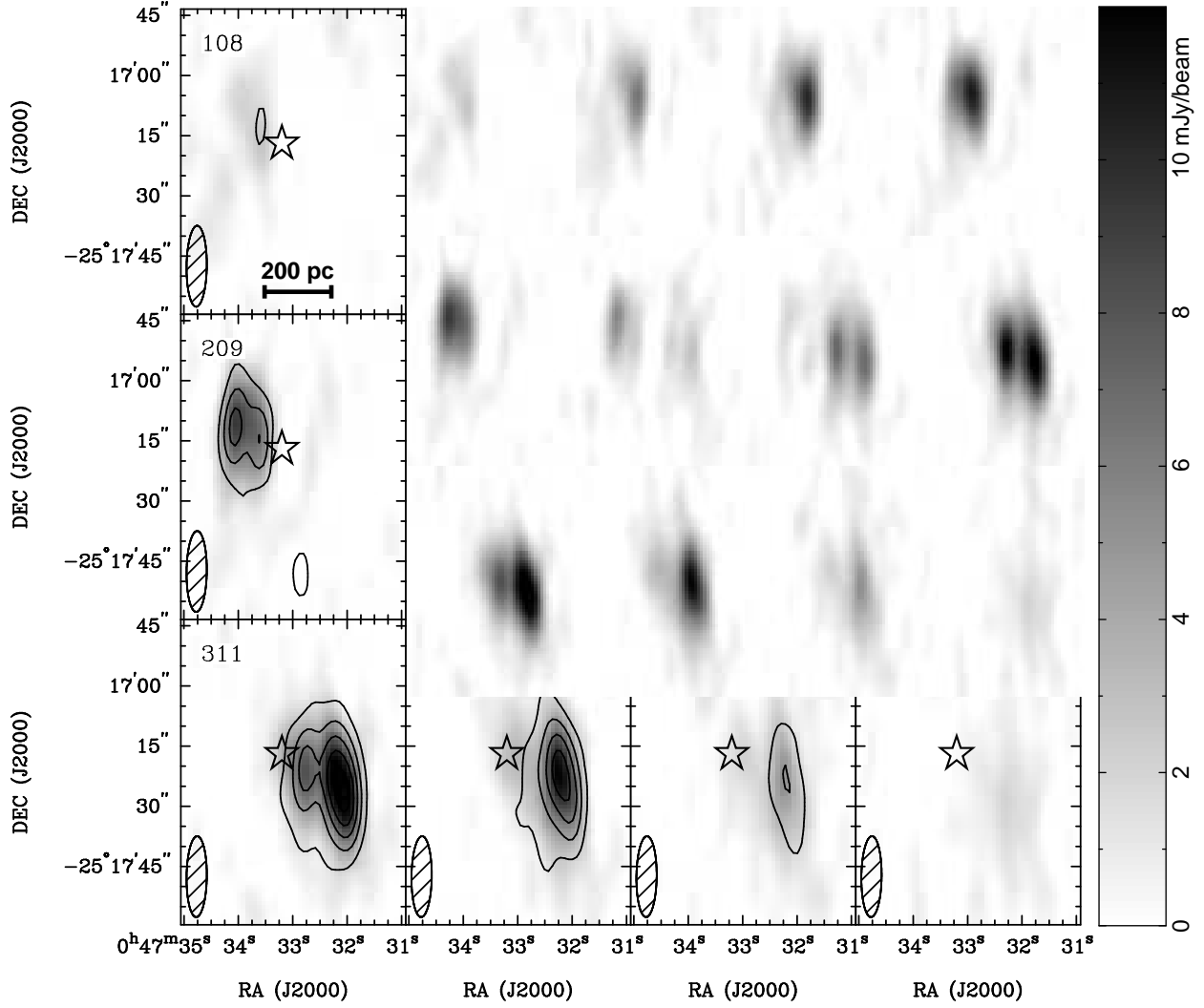


Fig. 1.— Channel maps of the naturally weighted  $\text{NH}_3(1,1)$  observations of the central region of NGC 253 with the  $\text{NH}_3(2,2)$  overlaid as contours (greyscale ranging from 0–12 mJy beam $^{-1}$ ; contours start at and are spaced by 2 mJy beam $^{-1}$ ). The star marks the peak of the 1.2 cm continuum which is coincident with the starburst center. The synthesized beam of the observations is shown in the lower left corner of each panel and the velocity is given in units of km s $^{-1}$  in the upper left corners. Each plot is an average over two channels which is about the velocity resolution of the Hanning smoothed data.

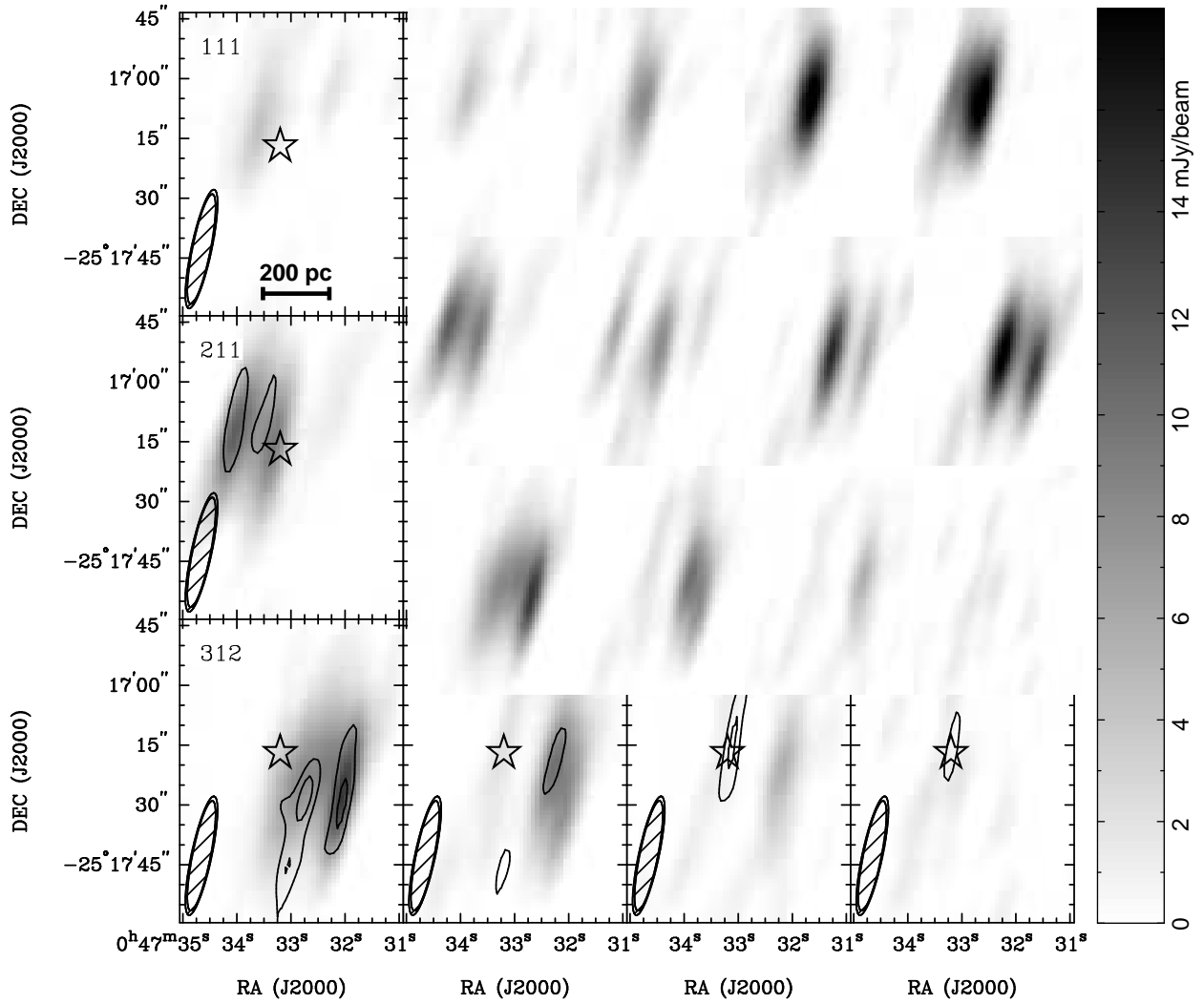


Fig. 2.— Channel maps of the naturally weighted  $\text{NH}_3(3,3)$  emission with  $\text{NH}_3(6,6)$  overlaid as contours (see also Fig. 1 for the symbols). Here the greyscale ranges from 0 to  $18 \text{ mJy beam}^{-1}$  and the contours start at  $2 \text{ mJy beam}^{-1}$  and are spaced by  $1 \text{ mJy beam}^{-1}$ .

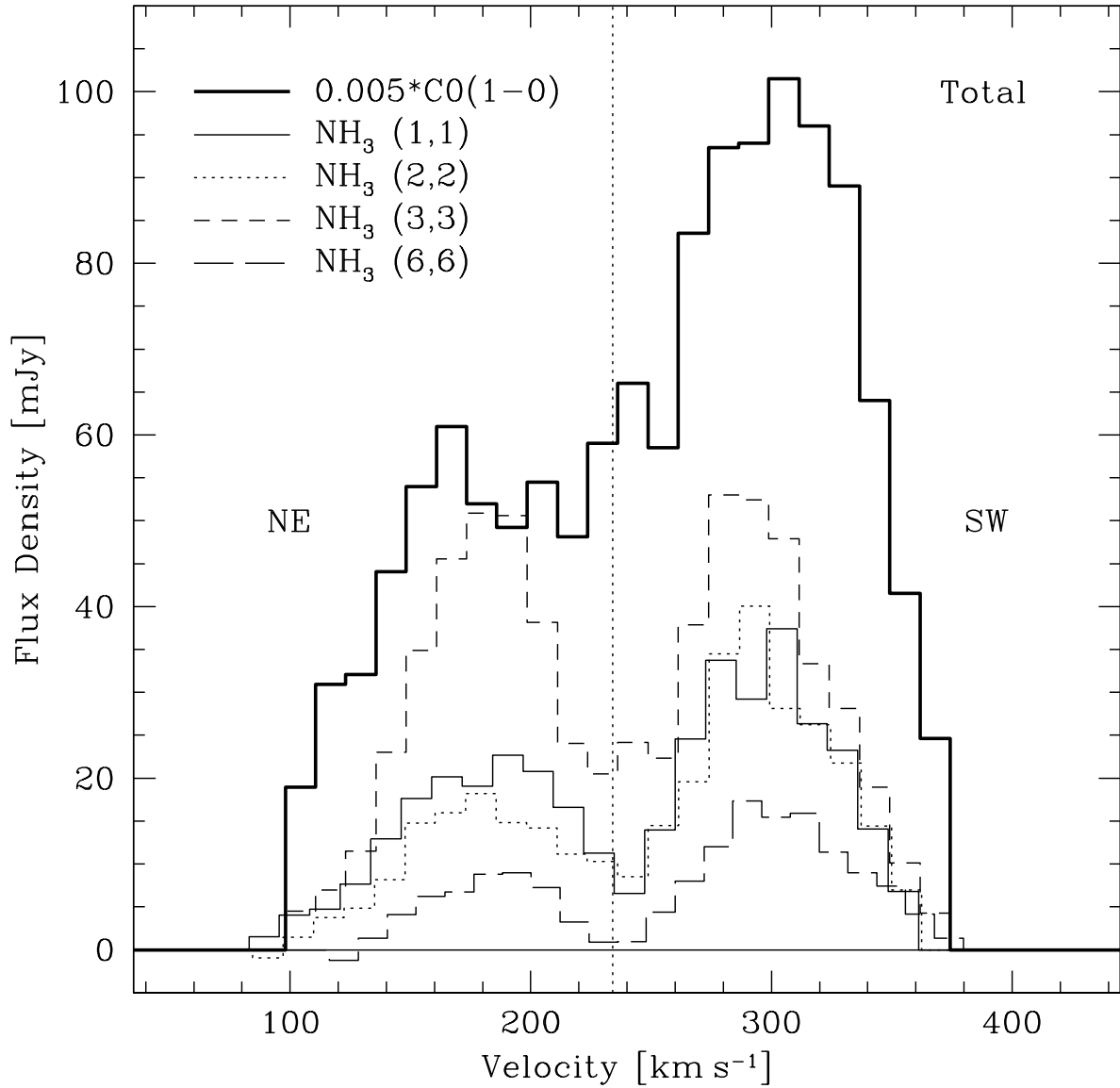


Fig. 3.— Total spectra of the ammonia inversion lines (see Fig. 4 for the corresponding maps) and the scaled (scaling factor 0.005) CO(1-0) transition in the inner  $\sim 600$  pc of NGC 253. The *vertical line* marks the systemic velocity of NGC 253.

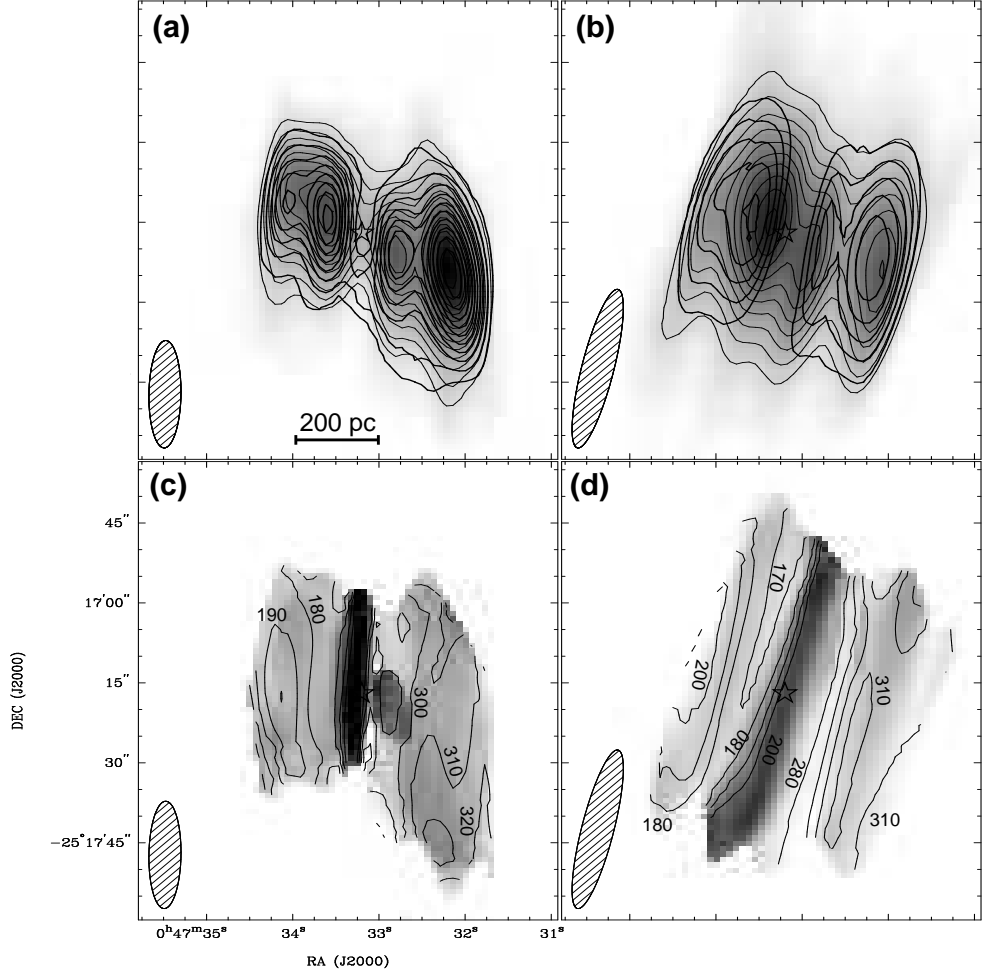


Fig. 4.— Moment maps of the ammonia emission in NGC 253. **(a)** Naturally weighted integrated intensity  $\text{NH}_3(1,1)$  emission, overlaid with its own contours (*thin*) and with contours of the  $\text{NH}_3(2,2)$  emission (*thick*). The data have been reduced using the full 12 hour uv-coverage. The greyscale is from 0 to  $30 \text{ K km s}^{-1}$  and the contours start at  $4 \text{ K km s}^{-1}$  and are spaced by  $2 \text{ K km s}^{-1}$ . **(b)** The  $\text{NH}_3(3,3)$  integrated emission again overlaid with its own contours (*thin*) and with contours of the restricted uv-coverage  $\text{NH}_3(1,1)$  emission (*thick* contours) in order to achieve the same beam size and position angle. The contours are at the same spacing and scale as in (a) and the greyscale ranges from 0 to  $25 \text{ K km s}^{-1}$ . **(c)** Velocity dispersion map of the  $\text{NH}_3(1,1)$  emission (full 12 h coverage) overlaid with contours of its velocity field. The greyscale range is  $20 - 70 \text{ km s}^{-1}$  and the contours of the velocity field are spaced by  $10 \text{ km s}^{-1}$ . Note that, for clarity, we do not show velocity contours in the central  $210 - 270 \text{ km s}^{-1}$  range. **(d)** The same as (c) but for the  $\text{NH}_3(3,3)$  emission. In all panels, the position of the 1.2 cm continuum source is marked by a *star* and the corresponding beams are shown in the lower left corners. All panels are on the same scale.

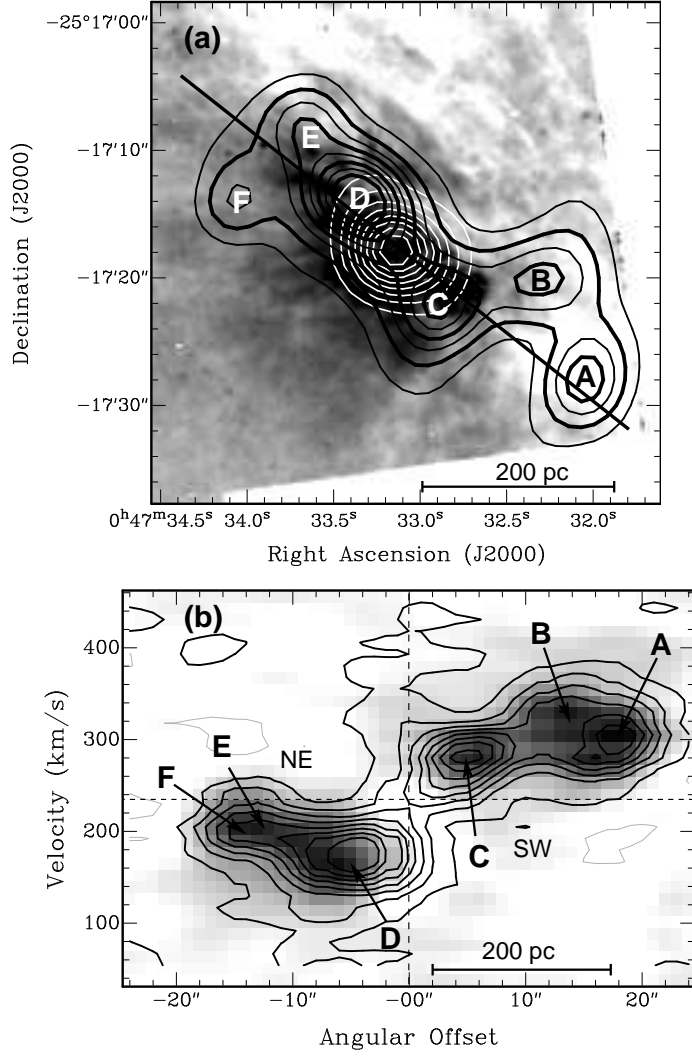


Fig. 5.— (a) Super-resolved  $\text{NH}_3(3,3)$  emission (resolution:  $5'' \times 5''$ ) displayed as *black contours* on a logarithmic HST/WFPC2 F814W image of the core of NGC 253. The contour levels start at and are spaced by  $10 \text{ K km s}^{-1}$ . The *white contours* show the  $1.2 \text{ cm}$  continuum emission. A position–velocity diagram along the major axis (*black diagonal line*) of the restricted uv-coverage  $\text{NH}_3(1,1)$  data with contours of  $\text{NH}_3(3,3)$  (contours start from 4% of the peak flux in steps of 10%) is shown in panel (b). Note that the data in the pV diagram are *not* super-resolved and, due to the elongated beam (see Fig. 4), all the molecular complexes are visible in this diagram even if they are offset from the black diagonal line in (a). The systemic velocity of NGC 253 and the position of the starburst center are shown as *dashed horizontal and vertical lines*, respectively. Positive angular offsets are toward the SW.

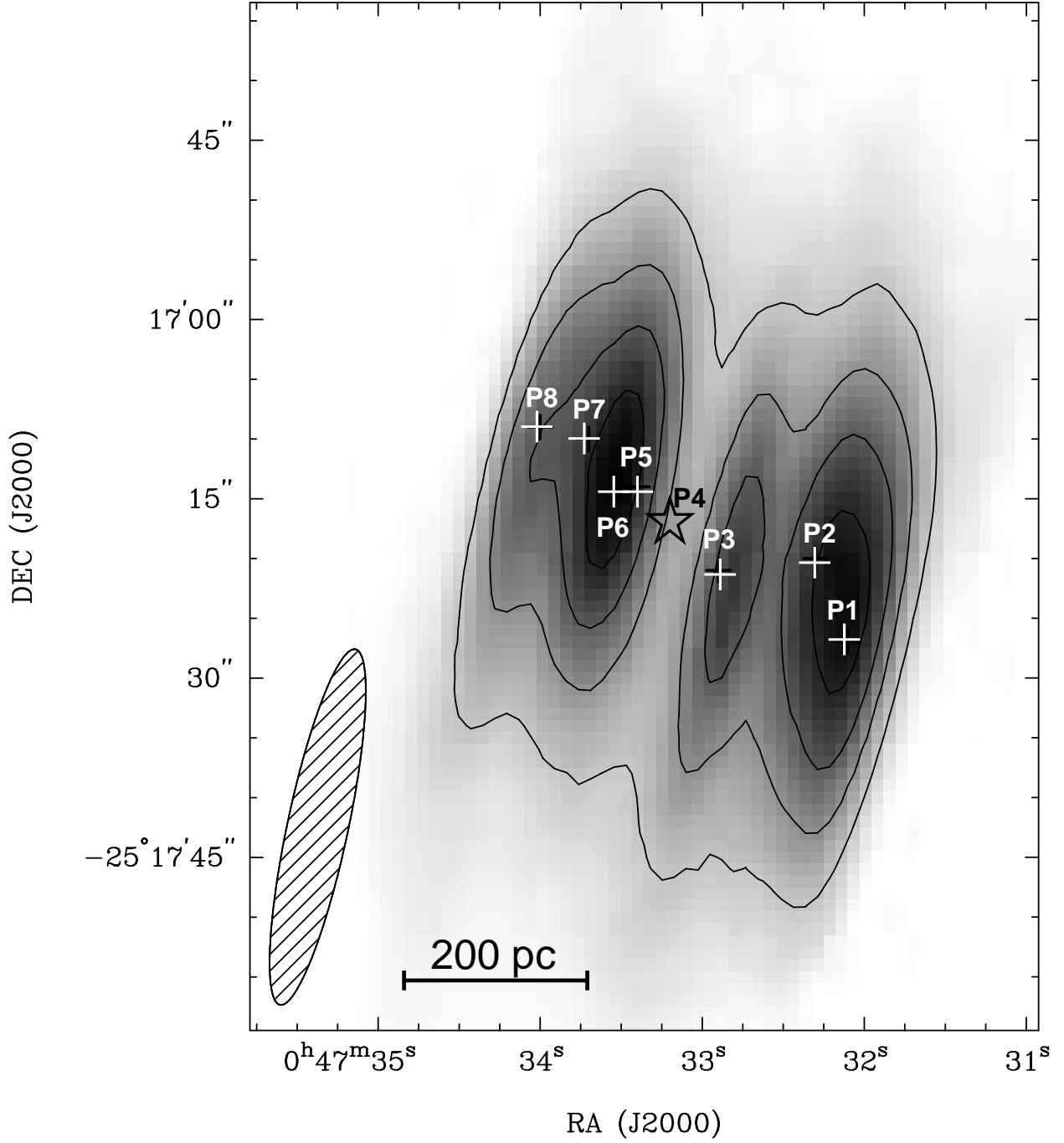


Fig. 6.— Total ammonia column density map and contours, computed by the sum of the column densities derived from NH<sub>3</sub>(1,1), (2,2), (3,3), and (6,6) [N<sub>1236</sub>(NH<sub>3</sub>)]. The contour levels start at and are spaced by  $1 \times 10^{14} \text{ cm}^{-2}$ . Overlaid are the locations of the positions P1 to P8 as *white crosses* and the 1.2 cm continuum peak, which corresponds to P4 as a *black star*. The size of the beam is shown in the lower left corner.

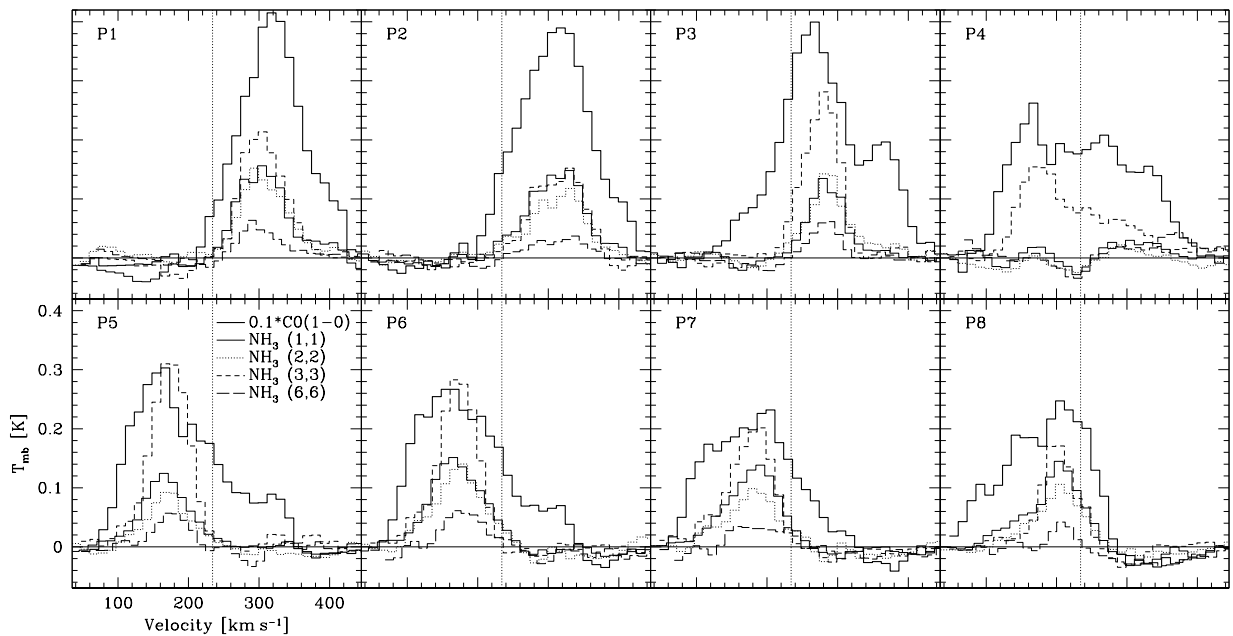


Fig. 7.— Ammonia spectra toward positions P1 to P8. Overlaid are corresponding CO spectra scaled by a factor of 0.1 (CO data courtesy of M. Dahlem and F. Walter ). Dotted vertical lines mark the systemic velocity of NGC 253.

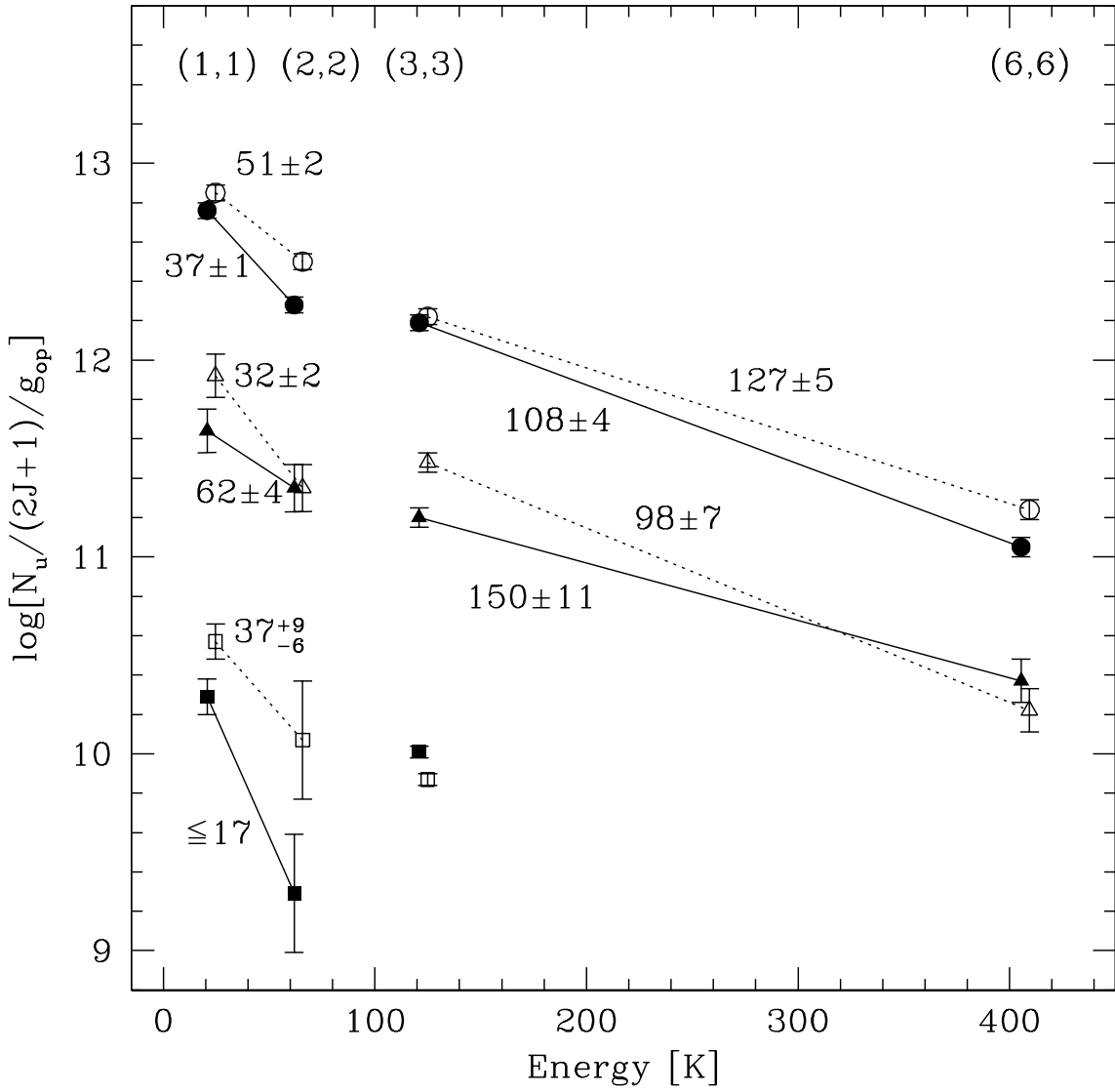


Fig. 8.— Boltzmann plot of the different ammonia transitions for the NE (*solid lines, filled symbols*) and SW (*dotted lines, open symbols*) molecular complexes. The horizontal axis denotes the energies of the levels above the ground state. The *circles* are our data, the *triangles* are taken from Mauersberger et al. (2003) and are *shifted down by one dex* on the vertical axis. The *squares* display the results from T02 *shifted down by two dex*. The numbers mark the rotational temperatures in K for the different slopes.

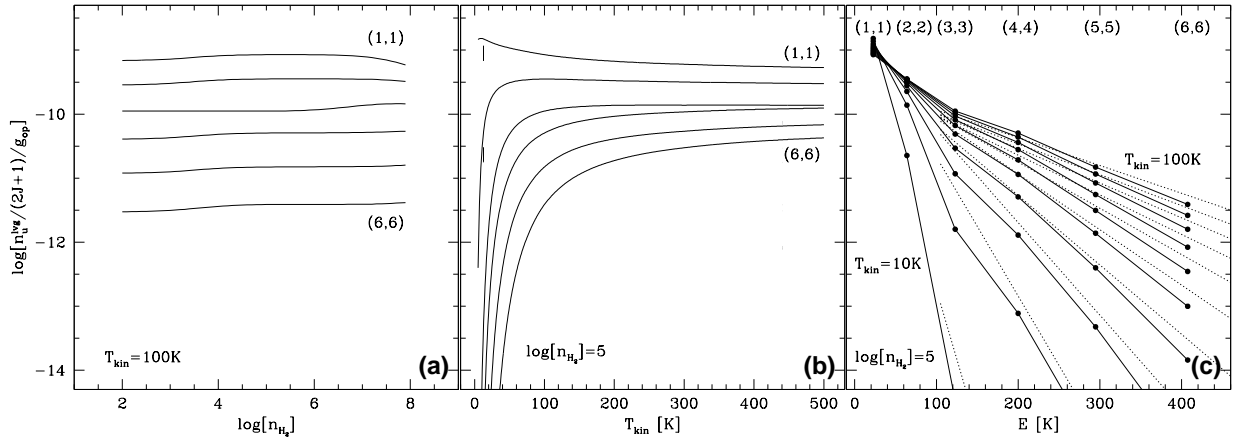


Fig. 9.— LVG models: Shown are upper level column densities (corrected for their individual statistical weights as used in Boltzmann plots) of NH<sub>3</sub>(1,1), (2,2), (3,3), (4,4), (5,5), and (6,6) as a function of (a) logarithmic H<sub>2</sub> volume density (kinetic temperature fixed at  $T_{\text{kin}} = 100\text{K}$ ), (b) kinetic temperature (at an H<sub>2</sub> density of  $10^5 \text{ cm}^{-3}$ ), and (c) the models of (b) as they appear in a Boltzmann plot (kinetic temperatures: 10–100 K, spaced by 10 K). The dotted lines mark the expected slopes if  $T_{\text{rot}}$  would be equal to  $T_{\text{kin}}$ . The LVG column densities can be converted into real column densities via eq. 5. The models shown are derived for a fractional NH<sub>3</sub> abundance relative to H<sub>2</sub> of  $10^{-8}$ , a velocity gradient of  $dv/dr = 1 \text{ km s}^{-1} \text{ pc}^{-1}$ , and  $o/p = 1$ . In panels (a) and (b) the models are displayed for the (1,1) to (6,6) inversion states from the top to the bottom, respectively.

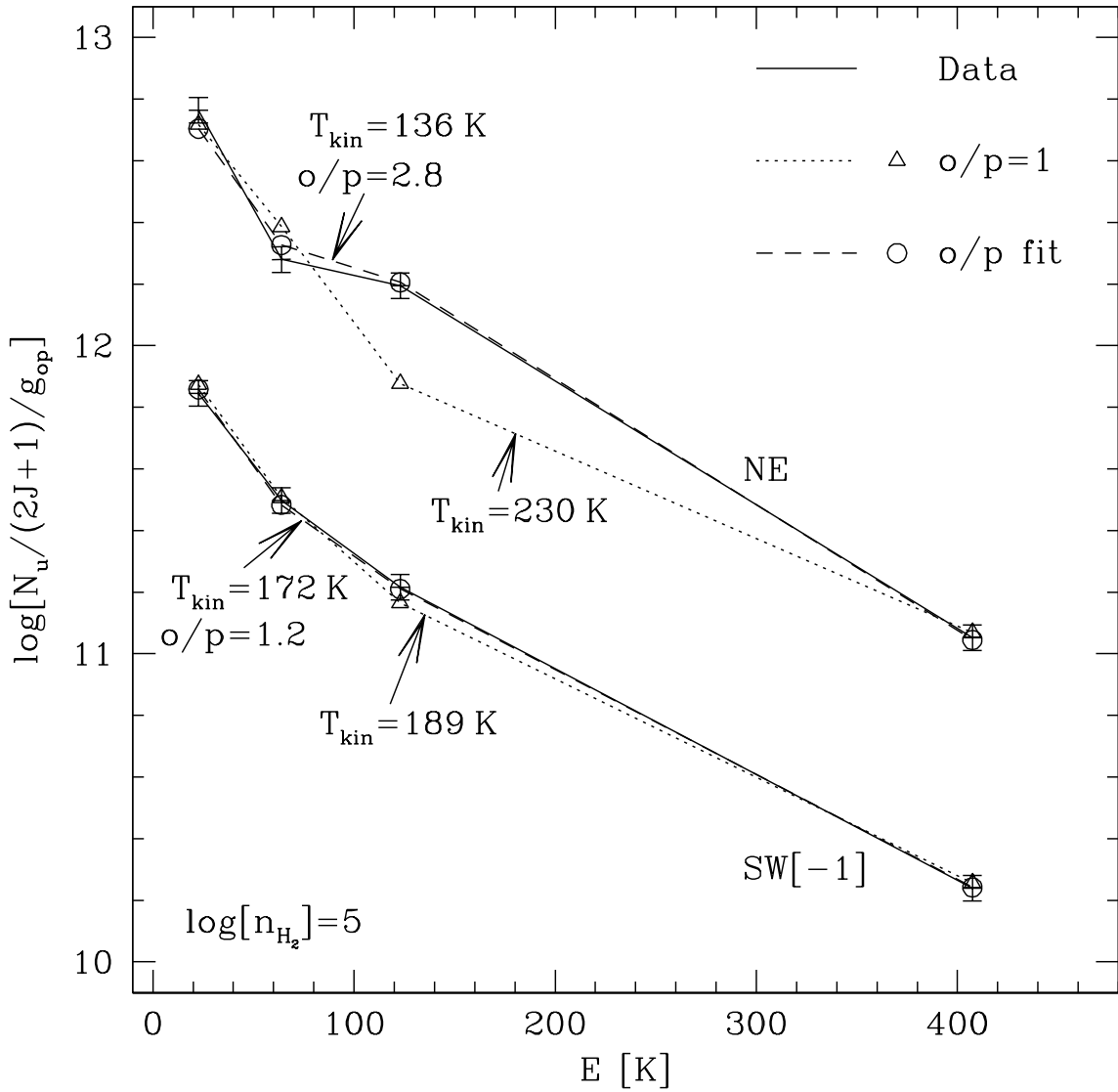


Fig. 10.— Comparison of one-temperature LVG models with  $o/p = 1$  and with fitted  $o/p$  ratios for the NE and SW regions. In the Boltzmann plots the *solid lines* connect the data points, whereas the *dotted lines* connect the modelled densities with  $o/p = 1$  (*triangles*). The *dashed lines* connect the results of the LVG fits with a variable  $o/p$  (*circles*). All points for the SW region are *shifted down by one dex*. Note that the models with varying  $o/p$  and the data points are very similar, in particular for the  $\text{NH}_3(3,3)$  measurements. The results of the different fits are labeled in the plot (see also Table 4).

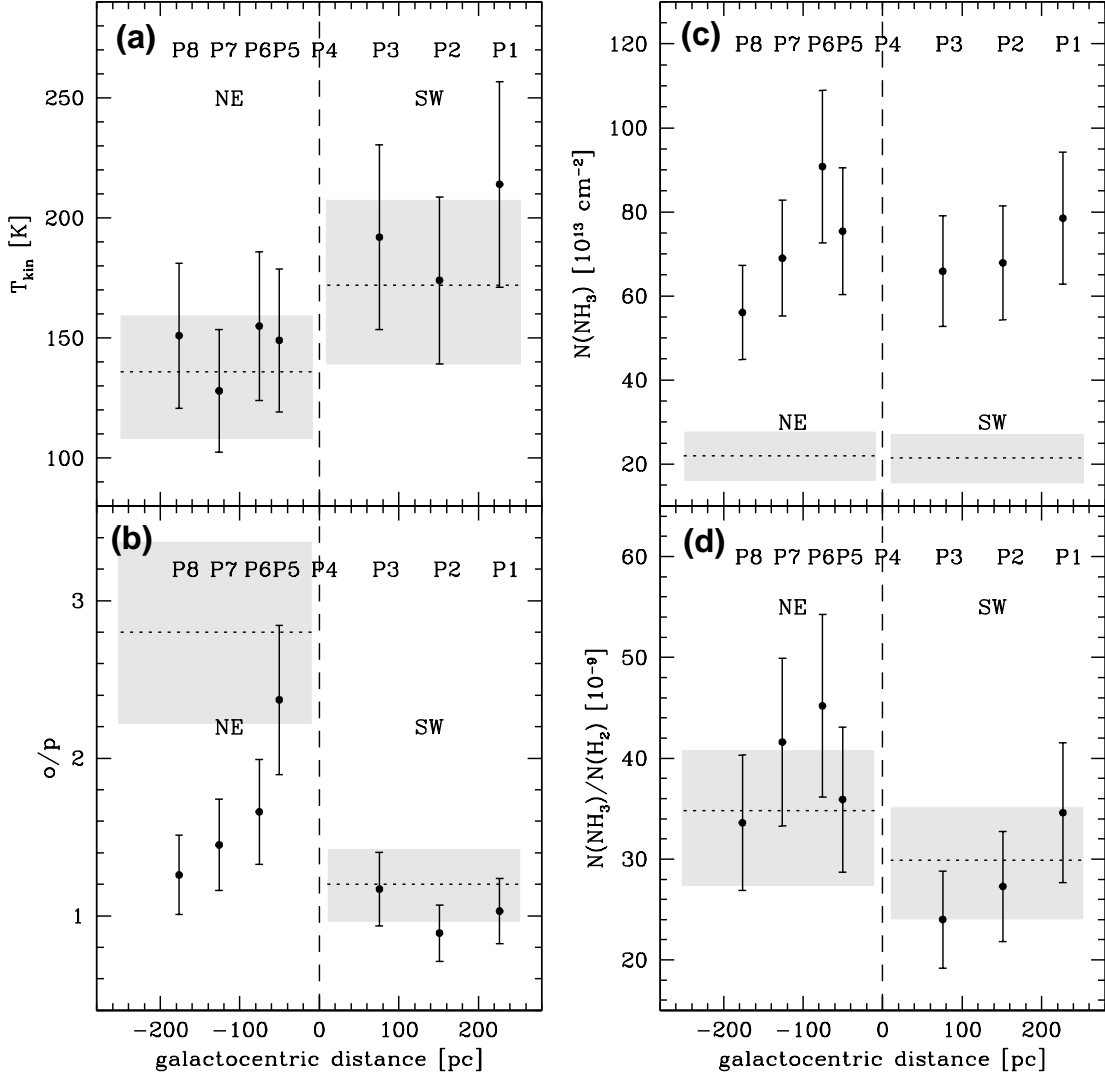


Fig. 11.— The results of the LVG fits to the data (see Table 4) as a function of galactocentric distance centered on the continuum peak of NGC 253 (vertical dashed line). The ordinates are: (a) the kinetic temperature, (b) the  $o/p$  ratio, (c) the total ammonia column density, and (d) the fractional ammonia abundance relative to  $\text{H}_2$ . The *dotted horizontal lines* mark the values derived for the entire NE and SW regions which also incorporate more diffuse emission. The errors of those values are displayed by the *grey boxes*.

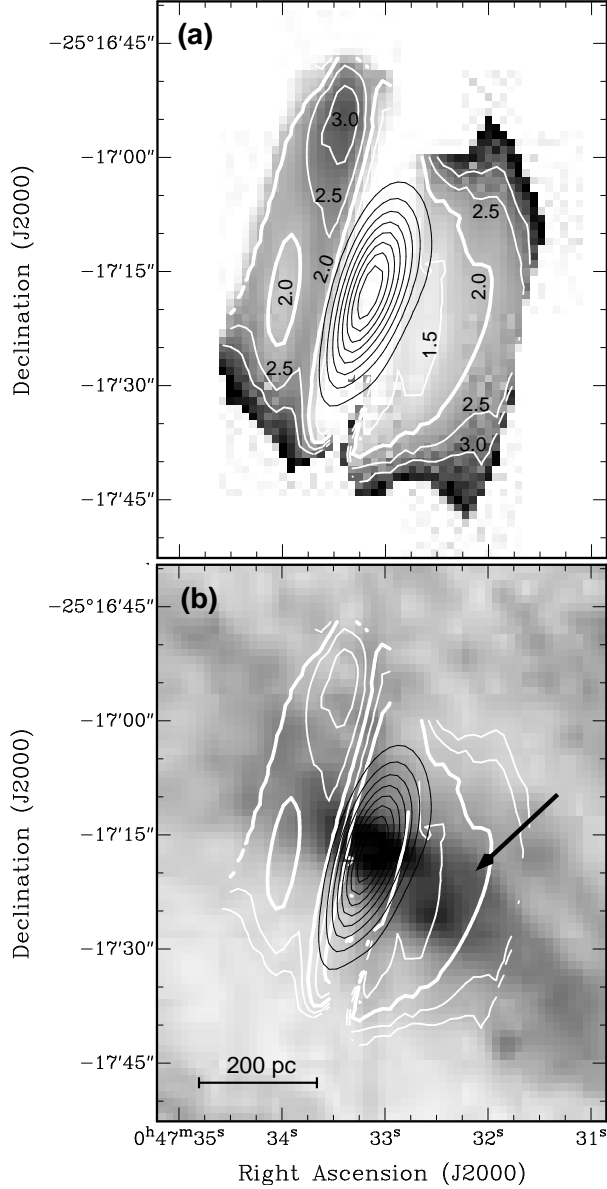


Fig. 12.— (a) Ammonia abundance map of NGC 253. The *white contours* are the ammonia abundances with respect to H<sub>2</sub> in units of  $10^{-8}$  (contours start at  $1.0 \times 10^{-8}$  and are spaced by  $0.5 \times 10^{-8}$ ). The *black contours* represent the 1.2 cm continuum emission. Note that this map is based on  $N_{1236}(\text{NH}_3)$  which underestimates the true abundances by  $\sim 1.5 - 2.5$  (see Sect. 4.4.4 and Fig. 6). The same contours are overlaid on a 2MASS  $J - K$  color map in panel (b) where dark colors are brighter in the K-band. The *black arrow* marks the position of the expanding shell around the X-ray point source shown in Fig. 13.

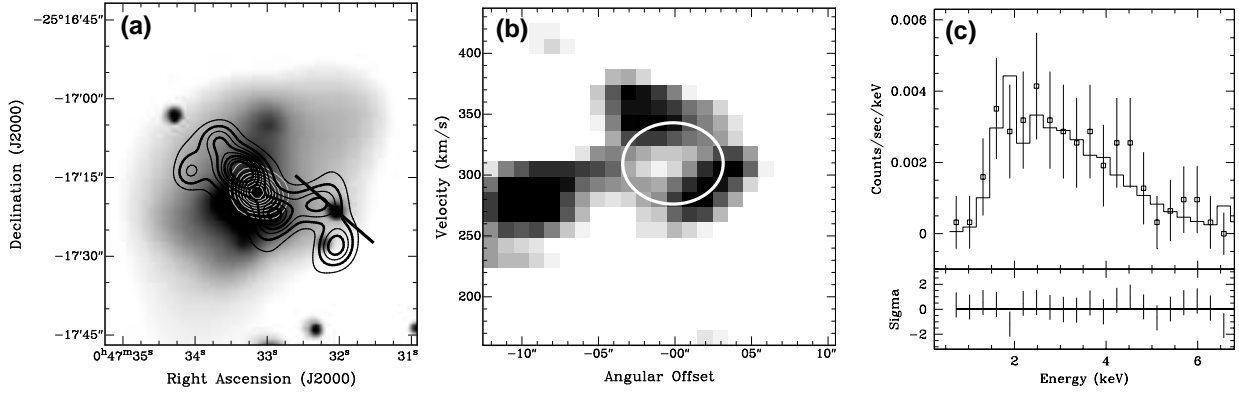


Fig. 13.— (a) The super-resolved  $\text{NH}_3(3,3)$  integrated intensity and 1.2 cm continuum map (as in Fig. 5) overlaid as contours on an adaptively smoothed 0.3–6.0 keV *Chandra* ACIS-S3 image of NGC 253. The position velocity (pV) diagram of the  $\text{NH}_3(3,3)$  data along the line positioned on the X-ray point source toward the west is displayed in panel (b). In the pV diagram an expanding shell feature is visible which is marked by the *white circle*. The *Chandra* spectrum of the X-ray point source is displayed in panel (c) with a fitted APEC thermal plasma model. The lower part of this panel shows the errors ( $[\text{Data}-\text{Model}]/\text{Error}$ ) of the fit.

Table 1. Global line properties of the ATCA ammonia observations for the NE, SW, and total regions ( $v_{\text{LSR,p}}$ : LSR peak velocity,  $\Delta v_{1/2}$ : line FWHM,  $\int S dv$ : integrated flux). The errors of the velocities are  $\sim 20 \text{ km s}^{-1}$  ( $\sim 40 \text{ km s}^{-1}$  for the [6,6] line due to the lower S/N ratio) and the fluxes are accurate to  $\sim 10\%$  ( $\text{NH}_3[6,6]$ : 20%).

Region	$v_{\text{LSR,p}}$ [km s $^{-1}$ ]	$\Delta v_{1/2}$ [km s $^{-1}$ ]	$\int S dv$ [Jy km s $^{-1}$ ]
$\text{NH}_3(1,1)$			
NE	191	94	2.00
SW	304	76	2.72
Total	...	...	4.72
$\text{NH}_3(2,2)$			
NE	178	86	1.48
SW	293	66	2.70
Total	...	...	4.18
$\text{NH}_3(3,3)$			
NE	180	63	3.91
SW	304	74	4.19
Total	...	...	8.10
$\text{NH}_3(6,6)$			
NE	179	60	0.60
SW	282	72	1.35
Total	...	...	1.95



Table 2. Ammonia and CO line parameters toward positions P1 to P8. The coordinates are given in the header of the table. The line parameters are as follows.  $T_{\text{mb},\text{p}}$ : peak main beam brightness temperature,  $v_{\text{LSR},\text{p}}$ : peak LSR velocity,  $\Delta v_{1/2}$ : line FWHM,  $\int T_{\text{mb}} dv$ : integrated brightness temperature. Note that for P4 the parameters are given for the absorption feature of  $\text{NH}_3(1,1)$ ,  $(2,2)$ ,  $(6,6)$  and for emission of  $\text{NH}_3(3,3)$  and  $\text{CO}(1-0)$ . The errors of the velocities are  $\sim 20 \text{ km s}^{-1}$  ( $\sim 40 \text{ km s}^{-1}$  for the  $[6,6]$  line), the fluxes are accurate to  $\sim 10\%$  ( $\text{NH}_3[6,6]$ : 20%).

Parameter	Unit	P1	P2	P3	P4	P5	P6	P7	P8
RA (J2000)	$00^h 47^m$	32 <sup>8</sup> 1	32 <sup>8</sup> 3	32 <sup>8</sup> 9	33 <sup>8</sup> 2	33 <sup>8</sup> 4	33 <sup>8</sup> 5	33 <sup>8</sup> 7	34 <sup>8</sup> 0
DEC(J2000)	$-25^\circ 17'$	27 <sup>''</sup>	20 <sup>''</sup>	21 <sup>''</sup>	17 <sup>''</sup>	14 <sup>''</sup>	14 <sup>''</sup>	10 <sup>''</sup>	09 <sup>''</sup>
$\text{NH}_3(1,1)$									
$T_{\text{mb},\text{p}}$	[K]	0.16	0.15	0.13	-0.03	0.12	0.15	0.14	0.14
$v_{\text{LSR},\text{p}}$	[ $\text{km s}^{-1}$ ]	304	330	279	228	165	165	190	203
$\Delta v_{1/2}$	[ $\text{km s}^{-1}$ ]	76	89	52	32	69	89	81	65
$\int T_{\text{mb}} dv$	[ $\text{K km s}^{-1}$ ]	13.38	14.37	8.43	-0.93	9.75	13.58	12.16	11.57
$\text{NH}_3(2,2)$									
$T_{\text{mb},\text{p}}$	[K]	0.15	0.12	0.14	-0.02	0.09	0.14	0.10	0.11
$v_{\text{LSR},\text{p}}$	[ $\text{km s}^{-1}$ ]	293	331	280	230	179	179	179	205
$\Delta v_{1/2}$	[ $\text{km s}^{-1}$ ]	67	91	50	52	64	68	63	63
$\int T_{\text{mb}} dv$	[ $\text{K km s}^{-1}$ ]	12.23	10.98	10.03	-1.19	6.60	11.31	8.35	7.95
$\text{NH}_3(3,3)$									
$T_{\text{mb},\text{p}}$	[K]	0.21	0.15	0.28	0.15	0.31	0.28	0.20	0.17
$v_{\text{LSR},\text{p}}$	[ $\text{km s}^{-1}$ ]	305	330	280	167	167	167	192	205
$\Delta v_{1/2}$	[ $\text{km s}^{-1}$ ]	63	89	63	113	67	62	70	51
$\int T_{\text{mb}} dv$	[ $\text{K km s}^{-1}$ ]	16.07	13.36	17.87	20.11	22.18	20.34	16.00	10.97
$\text{NH}_3(6,6)$									
$T_{\text{mb},\text{p}}$	[K]	0.06	0.04	0.06	-0.03	0.06	0.06	0.03	0.04
$v_{\text{LSR},\text{p}}$	[ $\text{km s}^{-1}$ ]	290	338	290	230	170	170	158	206
$\Delta v_{1/2}$	[ $\text{km s}^{-1}$ ]	53	78	41	48	54	66	94	36
$\int T_{\text{mb}} dv$	[ $\text{K km s}^{-1}$ ]	4.59	3.17	3.37	-1.47	3.54	4.5	3.12	1.62
$\text{CO}(1-0)$									
$T_{\text{mb},\text{p}}$	[K]	4.15	3.90	4.00	2.62	2.95	2.67	2.32	2.47
$v_{\text{LSR},\text{p}}$	[ $\text{km s}^{-1}$ ]	318	318	268	167	154	167	205	205
$\Delta v_{1/2}$	[ $\text{km s}^{-1}$ ]	94	114	89	226	138	137	151	139
$\int T_{\text{mb}} dv$	[ $\text{K km s}^{-1}$ ]	454.6	497.1	549.3	465.9	420.6	401.8	331.7	334.2



Table 3. Derived quantities of the ammonia inversion lines at positions P1 to P8 and the entire NE and SW regions.  $N_u$  are the column densities of the upper levels,  $N_{1236}(\text{NH}_3)$  are the combined measured column densities (assuming that the lower levels are as populated as the upper levels, but ignoring all contributions from other lines),  $N_{1236}(\text{NH}_3)/N(\text{H}_2)$  are the abundances based on the  $N_{1236}(\text{NH}_3)$  column densities.  $T_{12}$  and  $T_{36}$  are the rotational temperatures using the para-ammonia (1,1) and (2,2) and the ortho-ammonia (3,3) and (6,6) inversion lines, respectively. Whereas the absolute uncertainties of the column densities are  $\sim 10\%$ , ( $\text{NH}_3[6,6]$ : 20%) the relative uncertainties are  $\sim 5\%$ .  $T_{12}$  and  $T_{36}$  exhibit a statistical  $1\sigma$  error of 2 and 5 K, respectively.

Parameter	Unit	P1	P2	P3	P4 <sup>a</sup>	P5	P6	P7	P8	NE	SW
$N_u(1, 1)$	$[\times 10^{13} \text{ cm}^{-2}]$	8.78	9.42	5.53	9.9 <sup>a</sup>	6.39	8.91	7.98	7.59	1.74	2.10
$N_u(2, 2)$	$[\times 10^{13} \text{ cm}^{-2}]$	6.01	5.39	4.93	15.4 <sup>a</sup>	3.24	5.56	4.1	3.91	0.95	1.57
$N_u(3, 3)$	$[\times 10^{13} \text{ cm}^{-2}]$	6.97	5.80	7.76	8.73	9.63	8.83	6.94	4.76	2.19	2.30
$N_u(6, 6)$	$[\times 10^{13} \text{ cm}^{-2}]$	1.66	1.15	1.22	14.2 <sup>a</sup>	1.28	1.63	1.13	0.59	0.29	0.45
$N_{1236}(\text{NH}_3)$	$[\times 10^{13} \text{ cm}^{-2}]$	46.8	43.5	38.9	...	41.1	49.8	40.3	33.7	10.4	12.8
$N(\text{H}_2)$	$[\times 10^{21} \text{ cm}^{-2}]$	22.7	24.9	27.5	23.3	21.0	20.1	16.6	16.7	6.3	7.2
$N_{1236}(\text{NH}_3)/N(\text{H}_2)$	$[\times 10^{-9}]$	20.6	17.5	14.2	...	19.5	24.8	24.3	20.2	16.5	17.8
$T_{12}$	[K]	46	39	66	88 <sup>a</sup>	35	42	35	35	37	51
$T_{36}$	[K]	138	127	115	...	108	123	117	105	108	127

<sup>a</sup>The column densities listed for the  $\text{NH}_3$  (1,1), (2,2) and (6,6) absorption components are actually the ratio of the column density to the excitation temperature  $N/T_{ex}$  in units of  $10^{13} \text{ cm}^{-2} \text{ K}^{-1}$  (see Sect. 4.3).

Table 4. Results of the LVG model fits (excluding P4). Listed are the best parameters with a variable  $o/p$  ratio: the kinetic temperature  $T_{\text{kin}}$ , the ortho-to-para-ammonia abundance ratio ( $o/p$ ), the total ammonia column densities  $N(\text{NH}_3)$ , The ammonia abundances  $N(\text{NH}_3)/N(\text{H}_2)$ , and ammonia masses  $M(\text{NH}_3)$ . In addition we show the kinetic temperatures which are the results of fits with an  $o/p$  ratio of unity [ $T_{\text{kin}}(o/p = 1)$ ].

The errors are estimated to be  $\sim 20\%$ .

Parameter	Unit	P1	P2	P3	P5	P6	P7	P8	NE	SW
$T_{\text{kin}}$	[K]	214	174	192	149	155	128	151	136	172
$o/p$		1.0	0.89	1.2	2.4	1.7	1.5	1.3	2.8	1.2
$N(\text{NH}_3)$	$[\times 10^{13} \text{ cm}^{-2}]$	79.5	64.1	71.1	106	113	81.7	62.5	32.4	23.5
$N(\text{NH}_3)/N(\text{H}_2)$	$[\times 10^{-9}]$	34.6	27.3	24.0	35.9	45.2	41.6	33.6	34.8	29.9
$M(\text{NH}_3)$	$[\text{M}_\odot]$	...	...	...	...	...	...	...	9.0	9.8
$T_{\text{kin}}(o/p = 1)$	[K]	218	168	209	236	196	149	166	230	189